

Black Holes at the Centers of Nearby Dwarf Galaxies

Edward C. Moran¹, Karlen Shahinyan^{1,2}, Hannah R. Sugarman¹, Darik O. Vélez¹,
and Michael Eracleous^{3,4,5}

ABSTRACT

Using a distance-limited portion of the Sloan Digital Sky Survey (SDSS) Data Release 7, we have identified 28 active galactic nuclei (AGNs) in nearby ($d \leq 80$ Mpc) low-mass, low-luminosity dwarf galaxies. The accreting objects at the galaxy centers are expected to be intermediate-mass black holes (IMBHs) with $M_{\text{BH}} \leq 10^6 M_{\odot}$. The AGNs were selected using several optical emission-line diagnostics after careful modeling of the continuum present in the spectra. We have limited our survey to objects with spectral characteristics similar to those of Seyfert nuclei, excluding emission-line galaxies with ambiguous spectra that could be powered by stellar processes. The host galaxies in our sample are thus the least massive objects in the very local universe certain to contain central black holes. Our sample is dominated by narrow-line (type 2) AGNs, and it appears to have a much lower fraction of broad-line objects than that observed for luminous, optically selected Seyfert galaxies. Given our focus on the nearest objects included in the SDSS, our survey is more sensitive to low-luminosity emission than previous optical searches for AGNs in low-mass galaxies. The [O III] $\lambda 5007$ luminosities of the Seyfert nuclei in our sample have a median value of $L_{5007} = 2 \times 10^5 L_{\odot}$ and extend down to $\sim 10^4 L_{\odot}$. Using published data for broad-line IMBH candidates, we have derived an [O III] bolometric correction of $\log(L_{\text{bol}}/L_{5007}) = 3.0 \pm 0.3$, which is significantly lower than values obtained for high-luminosity AGNs. Applying this correction to our sample, we obtain minimum black-hole mass estimates that fall mainly in the $10^3 M_{\odot} - 10^4 M_{\odot}$ range, which is roughly where the predicted mass functions for different black-hole seed formation scenarios overlap the most. In the stellar mass range that includes the bulk of the AGN host galaxies in our sample, we derive a lower limit on the AGN fraction of a few percent, indicating that active nuclei in dwarf galaxies are not as rare as previously thought.

Subject headings: galaxies: active — galaxies: dwarf — galaxies: Seyfert

¹Astronomy Department, Wesleyan University, Middletown, CT 06459.

²Institute for Astrophysics, University of Minnesota, 116 Church St. S.E., Minneapolis, MN 55455.

³Department of Astronomy and Astrophysics, and Institute for Gravitation and the Cosmos, The Pennsylvania State University, 525 Davey Lab, University Park, PA 16802.

⁴Center for Relativistic Astrophysics, Georgia Institute of Technology, Atlanta, GA 30332.

⁵Department of Astronomy, University of Washington, Seattle, WA 98195.

1. Introduction

Numerous studies over the past two decades have revealed correlations between the masses of supermassive black holes (M_{BH}) and the large-scale properties of the galaxies within which they reside, such as the luminosity (e.g., Kormendy & Richstone 1995; Bentz et al. 2009), mass (Marconi & Hunt 2003), and velocity dispersion (σ_* ; Gebhardt et al. 2000; Ferrarese & Merritt 2000; Tremaine et al. 2002; Gültekin et al. 2009) of the stellar bulge. Based on these correlations, it is now widely presumed that supermassive black holes and the bulges of luminous galaxies grow and evolve in a coordinated manner via a single, common process. The case for the leading candidate, galaxy merging, is supported by simulations, which demonstrate that nuclear black hole growth occurs primarily through merger-induced accretion (Volonteri et al. 2003; Di Matteo et al. 2005; Hopkins et al. 2005). However, the matter is far from settled. In addition to the fact that some nearby late-type galaxies may lack central black holes (Gebhardt et al. 2001; Valluri et al. 2005), a number of critical issues remain unresolved. For example, do the scaling relations observed for bulge-dominated galaxies and supermassive black holes (e.g., $M_{\text{BH}}-\sigma_*$) apply in the low-mass regime? What are the origins of the black hole “seeds” that formed at earlier times, and what were their initial masses? Without answers to these questions, we lack a full understanding of the coordinated growth of black holes and galaxies, and, thus, a fundamental aspect of galaxy evolution.

Studies of nearby low-mass galaxies can provide key insight into these issues. Low-mass galaxies are likely to have had quiet merger histories, and the black holes at their centers, if present, are expected to be in the intermediate-mass range (i.e., $M_{\text{BH}} = 10^3\text{--}10^6 M_\odot$). Thus, the discovery of dwarf galaxies with massive central black holes affords the opportunity to explore black-hole/galaxy scaling relations in objects similar to the precursors of today’s large galaxies. Furthermore, as discussed by Volonteri et al. (2008), the present-epoch “occupation fraction” of black holes in galaxies — particularly those at the lowset masses — can be used to discriminate between seed formation scenarios, i.e., “light” seeds from Population III stellar remnants (Bromm et al. 1999) and “heavy” seeds formed from the collapse of metal-free gas in primordial galaxies (Lodato & Natarajan 2006). But in order for such investigations to succeed, two things are essential: (1) a determination of the demographics of massive black holes in the local universe, and (2) an accurate census of the properties of nearby galaxies that contain central black holes.

Much progress has been made recently in the identification and characterization of intermediate-mass black hole (IMBH) candidates and their host galaxies (Greene & Ho 2004, 2007b; Barth et al. 2004, 2005, 2008; Dong et al. 2007, 2012; Xiao et al. 2011; Jiang et al. 2011). However, as discussed by Greene & Ho (2007a), the search techniques used to select the objects for these studies have yielded samples that suffer to some degree from luminosity bias, resulting in incompleteness for both black holes and their hosts at low masses. In this paper, we report on the first of a series of projects designed to improve our understanding of the relationship between black holes and galaxies in the low-mass regime. Our approach and data selection methods are outlined in § 2. Host-galaxy photometry of our sample is described in § 3, and in § 4 we discuss the processing and analysis of the available nuclear spectroscopic data. Our survey has revealed a number of dwarf galaxies

that contain a central black hole (Moran 2010); their properties are presented in § 5. The paper concludes with a summary of our findings.

2. Sample Definition

2.1. A Distance-Limited Approach

Due to the small physical size of the sphere of influence of an IMBH and the limited resolving power of available instrumentation, dynamical methods for discovering (or setting upper limits on the masses of) such objects (Gebhardt et al. 2001; Valluri et al. 2005; Lora et al. 2009; Seth et al. 2010; Jardel & Gebhardt 2012; Neumayer & Walcher 2012) can only be employed for the very nearest galaxies (Ferrarese 2004). Thus, searches for IMBHs — even in the local universe — must rely on the detection of nuclear activity in a galaxy for evidence that a black hole is present. Unfortunately, owing to the fact that accretion luminosity depends in part on M_{BH} , active galactic nuclei (AGNs) with low-mass black holes tend to be faint. As a result, current samples of IMBH candidates are relatively small. The original and best-studied case is NGC 4395, a dwarf spiral galaxy that possesses a broad emission-line (type 1) nucleus (Filippenko & Sargent 1989) and a $\sim 10^5 M_{\odot}$ black hole (Filippenko & Ho 2003; Peterson et al. 2005). The other well-studied example is POX 52 (Barth et al. 2004; Thornton et al. 2008), which, despite being similar to NGC 4395 in terms of its black-hole mass and the optical and X-ray properties of its nucleus, is located in a dwarf spheroidal galaxy.

In recent years, a few hundred additional IMBH candidates have been identified using spectroscopic data from the Sloan Digital Sky Survey (SDSS; see Greene & Ho 2004, 2007b; Dong et al. 2007, 2012; Barth et al. 2008; Reines et al. 2013). The samples of Greene & Ho (2004; 2007b) and Dong et al. (2012) were limited to broad-line AGNs, since black-hole mass estimates can be made for them. The Barth et al. (2008) and Reines et al. (2013) surveys targeted lower mass host galaxies, yielding samples dominated by narrow-line (type 2) AGNs. Although all of these studies were successful at demonstrating the existence of IMBHs in other galaxies, the relatively high signal-to-noise (S/N) ratio thresholds they required, coupled with the fact that the SDSS is essentially a flux-limited survey, introduced luminosity bias into their AGN samples. For example, nuclear luminosity (indicated by the strength of the [O III] $\lambda 5007$ emission line) appears to correlate with distance in the Greene & Ho (2004) and Barth et al. (2008) samples. This arises in circumstances where low-luminosity objects are too faint to be detected at large distances, and high-luminosity objects are too rare to be found within a small local volume. The net effect for the IMBH samples is that their nuclear luminosity distributions, compared to the [O III] luminosity function, are shifted to higher values.

Evidently, the host galaxies of emission-line selected IMBH candidates in the first SDSS surveys are biased to higher luminosities as well. As pointed out by Greene & Ho (2007a) and Barth et al. (2008), galaxies must be sufficiently bright to be targeted for spectroscopy in the SDSS. Given

the distances of the objects in these samples (the median redshift of the Greene & Ho sample is $z \approx 0.10$), this translates to relatively high luminosities (and masses) for the IMBH host galaxies. The objects included in the Greene & Ho (2004; 2007b) and Barth et al. (2008) surveys are typically ~ 1 mag fainter than L^* , but very few are faint enough to qualify them as dwarf galaxies similar to NGC 4395 and POX 52.

The presence of luminosity bias in existing IMBH samples could mean that the low-mass limits for central black holes and/or their host galaxies have not yet been reached. If this is the case, we lack crucial information about the very objects that could provide the greatest leverage (via their black hole occupation fraction) on the massive black-hole seed formation mechanism. The goal of the project described here, therefore, is to investigate whether or not weaker AGNs can be identified in even less-luminous galaxies. The success of the surveys cited above demonstrates that even at low values of M_{BH} emission-line diagnostics remain a powerful tool for identifying AGNs. We have therefore adopted this strategy as well. However, the approach of our survey differs in an important way: rather than selecting objects based on their spectral properties, we instead assemble a sample of all potential AGN host galaxies within a certain distance limit and *then* search each for emission-line evidence of black-hole accretion. Our focus is on the nearest objects (1) to enable the detection of weak active nuclei in the faintest (and least massive) host galaxies, and (2) to maximize the sensitivity of any follow-up observations. As we discuss below, our sample provides the best coverage to date of the lower portions of both the nuclear and host-galaxy luminosity functions.

2.2. Data Selection

As with the prior emission-line searches for IMBH candidates listed above, the data for our survey are drawn from the SDSS. In its seventh data release (DR7; Abazajian et al. 2009), the spectroscopic portion of the SDSS covers $\sim 8200 \text{ deg}^2$ of sky, primarily in the North Galactic Cap. We began by selecting all objects in the DR7 that have (1) extragalactic spectral classifications (i.e., star and sky spectra were omitted, but objects with “unknown” classifications were included) and (2) heliocentric recessional velocities of $v_r \leq 5300 \text{ km s}^{-1}$ (i.e., $z \leq 0.0177$). The velocity limit was adopted based on our rough estimates that objects like NGC 4395 would just be included in the SDSS at the corresponding distance (galaxies must be brighter than $r = 17.77$ mag for SDSS spectroscopy) or that we would be able to observe them with medium-aperture telescopes if they were not. We corrected the recessional velocities for infall due to the Virgo cluster and Great Attractor following Mould et al. (2000), with an adjustment for the Local Group component described by Karachentsev & Makarov (1996). Physical distances to the objects were derived from their corrected velocities by applying the Hubble Law with $H_0 = 73 \text{ km s}^{-1} \text{ Mpc}^{-1}$. For the majority of the sample, the adopted velocity limit corresponds to a maximum distance of ~ 80 Mpc. The distances of objects with the lowest redshifts and those that lie in the direction of the Virgo cluster have the greatest uncertainty; as discussed below in § 5.1, the distances of all AGNs in our sample have been closely scrutinized to ensure that our assessments of their luminosities and

masses are as accurate as possible.

This selection produced an initial sample of over 10^4 spectra. However, a problem encountered with nearby galaxies is that, quite frequently, extranuclear regions have been observed spectroscopically by the SDSS rather than (or in addition to) the nucleus or central region of the galaxy. We decided that visual inspection of SDSS images indicating the placement of the spectral fiber was the most reliable (though certainly not the most expedient) method of identifying and eliminating extranuclear spectra. The process was straightforward for the most part, but for irregular galaxies and small, knotty galaxies at large distances it was sometimes unclear if an object’s “central” region had been observed. These were evaluated case-by-case; in the end, we kept the spectra only when we felt that an attempt to reobserve the galaxy would not result in a better characterization of its nucleus.

In total, the filtering process yielded a final sample of 9,526 galaxies. We then acquired their photometric data from the SDSS to identify low-mass galaxies (§ 3), and processed and analyzed their spectra to search for nuclear activity in the objects (§ 4).

3. SDSS Photometry

Accurate photometry is critical for this project in order to establish the properties of any black-hole host galaxies we uncover and to characterize the parent sample as a whole. For the vast majority of objects in our sample, the photometric data available from the SDSS provide a reliable measure of a galaxy’s brightness. Whenever possible, we have employed the SDSS Petrosian magnitudes, which are derived from aperture photometry; they are independent of surface brightness modeling and afford the most direct comparison between our sample and the samples examined in previous IMBH surveys (e.g., Greene & Ho 2004; Barth et al. 2008).

We note, however, that in some instances errors are present in the SDSS photometry. For our sample of nearby galaxies, this seems to involve primarily two types of objects: very extended galaxies, and less extended objects that lie close in projection to a bright foreground star. Photometry problems can be revealed by examining the SDSS photometric pipeline’s object flags and/or by noting significant discrepancies when various types of SDSS magnitudes are compared, e.g., the Petrosian and “model” magnitudes (which are obtained by fitting an exponential or de Vaucouleurs model to a galaxy’s surface brightness profile), or the DR7 magnitudes and those recalculated as part of the DR8 (Aihara et al. 2011). Unfortunately, it is not automatically clear which set of measurements (if any) should be preferred when a problem is suspected. Therefore, as discussed in § 5.1, we carefully scrutinized the photometry data available for any objects identified as AGNs.

An accurate characterization of our overall galaxy sample is possible if we temporarily ignore objects with suspected photometry problems and those with the greatest relative uncertainties in their distances (i.e., objects with the lowest redshifts [$z < 0.003$] and potential members of the Virgo cluster; see Mould et al. 2000). Such exclusions reduce our sample by only $\sim 12\%$. The

absolute magnitude and stellar mass distributions for the 7415 remaining galaxies are displayed in Figure 1. Absolute magnitudes were computed using our distance estimates (§ 2.2) and the SDSS g -band magnitudes (which are best for comparison to the Greene & Ho and Barth et al. samples). We estimated the stellar masses of the galaxies following the method of Bell et al. (2003), which combines a galaxy’s luminosity with a mass-to-light ratio derived from a color measurement. Our calculations employ the $g - r$ colors and i -band luminosities. As Figure 1 indicates, our distance-limited sample is dominated by dwarf galaxies fainter than $M_g = -18$ and less massive than $10^{10} M_\odot$ — the very population we wish to search for evidence of nuclear activity.

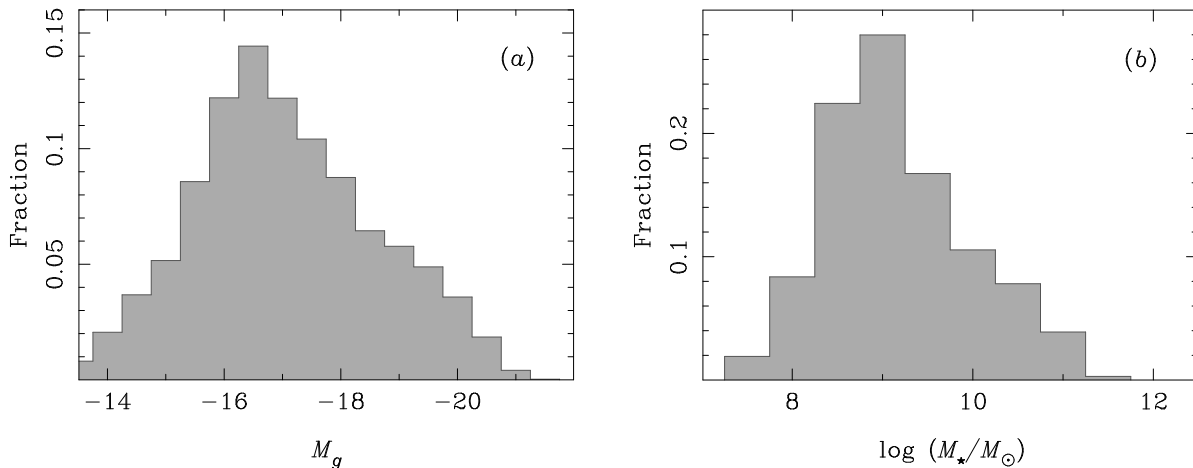


Fig. 1.—(a) Absolute g magnitude and (b) stellar mass distributions for our SDSS DR7 sample of nearby galaxies.

4. SDSS Spectroscopy

Optical spectra of the galaxies in our sample were acquired from the SDSS DR7 database (Abazajian et al. 2009). The spectra, obtained using fibers that provide an effective $3''$ diameter aperture, span a wavelength range of ~ 3800 – 9200 Å at a resolving power of $\lambda/\Delta\lambda \approx 2000$. Two types of analysis were performed in order to evaluate the nuclear activity of each object: (1) subtraction of the stellar continuum present in the raw spectrum, and (2) measurement of the fluxes of the important diagnostic emission lines.

4.1. Continuum Modeling

Regardless of whether the galaxies in our sample are AGNs, their nuclear spectra are almost always dominated by starlight from their central regions. The superposition of absorption features in the stellar continuum and nebular emission lines principally affects the apparent strengths of

the narrow Balmer lines. However, depending on the stellar population present and the relative strength of the line emission, the apparent fluxes of some important diagnostic forbidden lines can be affected as well. In addition, when host-galaxy emission dominates, it can mask the presence of weak, broad emission lines associated with an active nucleus. Thus, as discussed by Ho (2008), careful subtraction of the stellar continuum is essential for an accurate emission-line assessment of an object’s nuclear activity.

Our initial analysis employed the continuum-fitting code developed by Eracleous & Halpern (2001). After masking out the locations of strong emission lines, the program constructs a continuum model for each galaxy spectrum by fitting a linear combination of starlight templates and a non-stellar power-law component. The emission-line flux ratios in the residual spectrum (obtained by subtracting the continuum model from the data) are then used to classify the galaxies (Veilleux & Osterbrock 1987; Kewley et al. 2006). The program was designed to use absorption-line galaxy spectra as templates, as these often accurately represent the stellar populations and velocity dispersions present in the centers of emission-line galaxies. A search for suitable templates among the SDSS DR7 spectra obtained for this project yielded a set of over 30 spectra that have very high S/N and appear to be devoid of emission lines. Using these templates, we were able to identify the majority of AGNs located in the higher mass galaxies from our sample. However, two concerns arose regarding the effectiveness of this approach for weak-lined dwarf galaxies. First, many dwarf galaxies have bluish stellar continua with effective spectral types of G, F, or even A stars. High-quality spectra of nearby galaxies that have similar colors but no emission lines are extremely rare in the DR7, so our template set was very incomplete for such objects. Second, many of the best templates we selected were associated with fairly massive galaxies whose stellar velocity dispersions are larger than those of dwarf galaxies, which might lead to improper subtractions in the vicinities of important diagnostic emission lines.

To address these issues, we also analyzed the data with the GANDALF package (Sarzi et al. 2006; Sarzi et al. 2007). GANDALF operates in two stages. Similar to the approach described above, it first obtains an initial model for the continuum by masking off emission lines and then using the pPXF software (Cappellari & Emsellem 2004) to fit a linear combination of starlight templates that has been multiplied by a low-order polynomial (to account for reddening and flux-calibration differences between the object and template spectra) *and* broadened to match the line-of-sight velocity dispersion of the galaxy. GANDALF then lifts the masks and fits the emission lines simultaneously with the continuum. We used synthetic stellar population (SSP) models based on v. 9.1 of the MILES stellar library as starlight templates (Vazdekis et al. 2010); for a given prescription of the initial mass function (IMF) and metallicity, these models are calculated for 50 ages between 0.063 Gyr and 17.8 Gyr. The spectral resolution of the templates we used is $\sigma = 64$ km s^{−1}. GANDALF fits are generally excellent, with values of χ^2 per degree of freedom of \sim unity or less. Tests using a set of ~ 30 galaxy spectra with a range of emission-line strengths indicated that the two continuum-subtraction programs yield similar results for objects with strong emission lines, but for weak-lined objects we generally obtained smoother residuals and hence more reliable

emission-line fluxes with GANDALF. An example of continuum fitting with GANDALF is displayed in Figure 2. For analysis of the full sample, we employed MILES templates generated for a Kroupa (2001) universal IMF and solar metallicity; these yielded the best results for a test set of low-mass ($\sim 10^9 M_\odot$) galaxies.

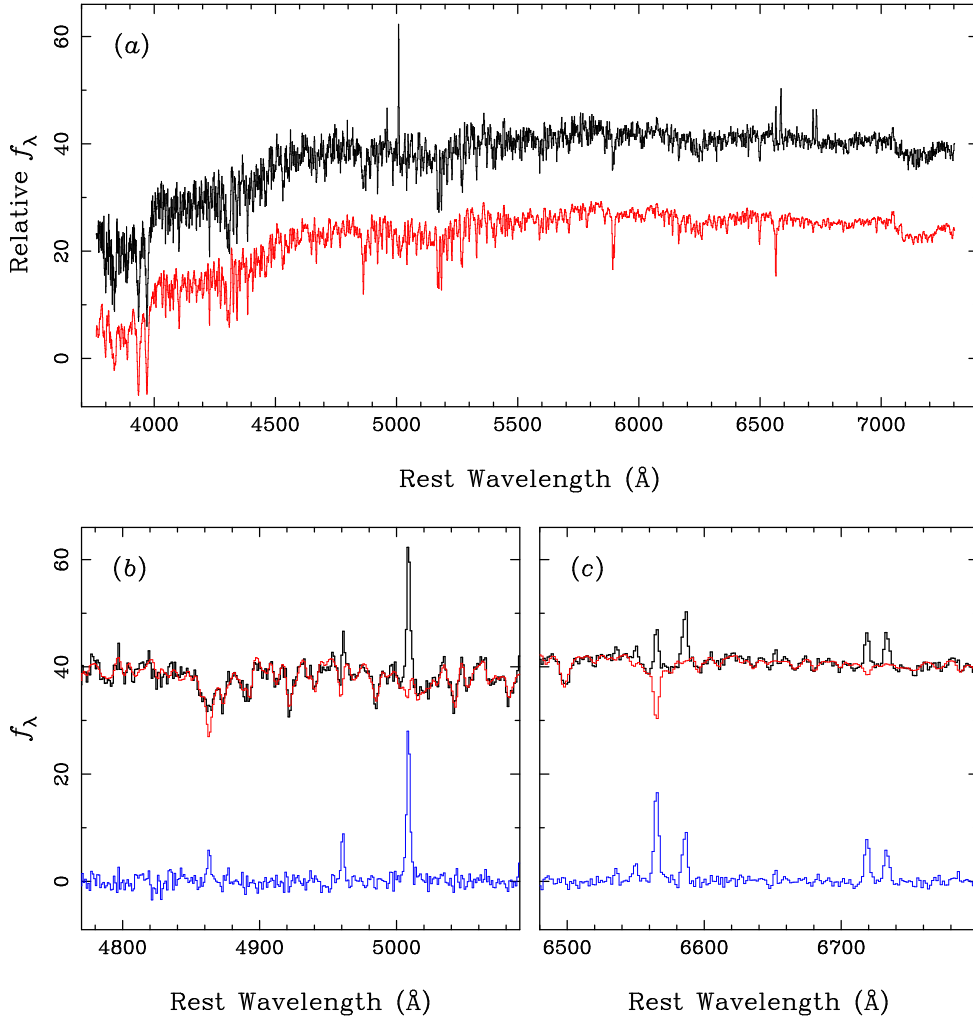


Fig. 2.—Continuum modeling of the spectrum of J0802+1032, which falls below the median for our dwarf galaxy AGN sample in terms its overall S/N ratio and emission-line equivalent widths. In (a), the original SDSS spectrum (black) and best-fit continuum from GANDALF (red, offset for clarity) are displayed. In the lower panels, the continuum fit (red) is overlaid on the original spectrum (black) in the vicinity of (b) H β λ 4861 (including [O III] $\lambda\lambda$ 4959, 5007) and (c) H α λ 6563 (including [N II] $\lambda\lambda$ 6548, 6583 and [S II] $\lambda\lambda$ 6716, 6731). The emission-line flux ratios revealed in the residuals from the continuum subtraction (blue) indicate the presence of an active nucleus.

4.2. Emission-Line Measurements

As mentioned above, GANDALF fits the emission lines simultaneously with the continuum, so line fluxes (and fully propagated errors associated with the fits) are obtained automatically. This is achieved with a set of user-specified emission-line constraints that allow one to define the profiles and relative rest-frame wavelengths of lines, fix the flux ratios of multiplets (e.g., [O III] $\lambda\lambda 4959, 5007$), and associate the velocity widths of various lines. For the analysis of the full sample, we (a) assumed that the lines have Gaussian profiles and (b) tied the velocity widths of forbidden lines to a common value that is allowed to differ from that of the permitted lines (H and He). This set-up works well for the majority of narrow emission-line galaxies.

However, as discussed by Oh et al. (2011), GANDALF does not always achieve acceptable fits for SDSS spectra. Moreover, no single set of assumptions about the continuum templates or emission-line properties is appropriate for all objects. Inaccuracies in automatically measured line fluxes can occur whenever the continuum or line profiles are not properly modeled, especially for weak-lined objects. Thus, we have taken additional steps to verify the accuracy of the line-flux measurements. Our main goal is to ensure that no potential AGN candidates have been overlooked.

To do this, we visually inspected the continuum fitting results for the entire sample. First, we constructed a residual spectrum for each object by subtracting the continuum model obtained with GANDALF from the original data. Ideally, this should contain any emission lines present and a continuum with a mean of zero that reflects the noise in the raw data and errors associated with the fit. We examined each residual spectrum using three-paneled plots that show the full wavelength range and close-ups of the $H\alpha$ and $H\beta$ regions. Poor continuum or emission-line fits are easily spotted this way, and the experienced eye can quickly recognize subtle AGN features that would be difficult to identify as completely and efficiently in an automated manner. We also examined a “noise” spectrum for each galaxy constructed by subtracting the total model (continuum plus emission lines) from the data. Residuals in the noise spectrum at the positions of emission lines indicate objects with non-Gaussian line profiles.

We adopted GANDALF line-flux measurements for objects whose residual spectrum is reasonably flat in the continuum and whose noise spectrum exhibits no strong features at the positions of the diagnostic emission lines. If these conditions were not met, or if something in the residual spectrum suggested that an AGN may be present, we analyzed the data further. For objects with poor continuum fits, we refitted the spectra in GANDALF using templates with non-solar metallicity, including a non-stellar power law ($F \propto \nu^{-\alpha}$, with $\alpha = 1 - 2$) as one of the templates, and/or including broad Balmer-line components in the emission-line fits. In some instances, increasing the order of the multiplicative polynomial applied to the templates was necessary to eliminate low-frequency wiggles in the residual continuum. For objects with non-Gaussian line profiles, we either added more emission components in follow-up GANDALF fits or used the *splot* task in IRAF to remeasure the fluxes of lines by directly integrating residual spectrum. The latter approach was best for narrow-line objects with Lorentzian or Voigt line profiles. And finally, for AGN candidates

selected visually, we carefully reexamined all of the information contained in the spectrum (e.g., the velocity widths of various lines or the presence of lines with high ionization potentials) and remeasured the emission-line fluxes.

4.3. Upper and Lower Limits

The visual inspection of the continuum-fitting results described above revealed some potential AGN candidates that lack detections of one or more of the lines useful for diagnosing nuclear activity. For example, we noticed a number of objects with strong [O III] $\lambda 5007$ emission for which the weaker H β line is not detected. For these objects, we measured the flux in 40–50 independent bins on either side of [O III] + H β in the residual spectrum. The widths of the bins were set to be roughly equal to the width of [O III] $\lambda 5007$ near its base. We then computed H β upper limits as three times the RMS of the flux in the continuum bins. As a safety check, we overplotted the results on the residual spectrum to ensure that the derived limits are consistent with the noise levels in the spectra. Two examples are shown in Figure 3.

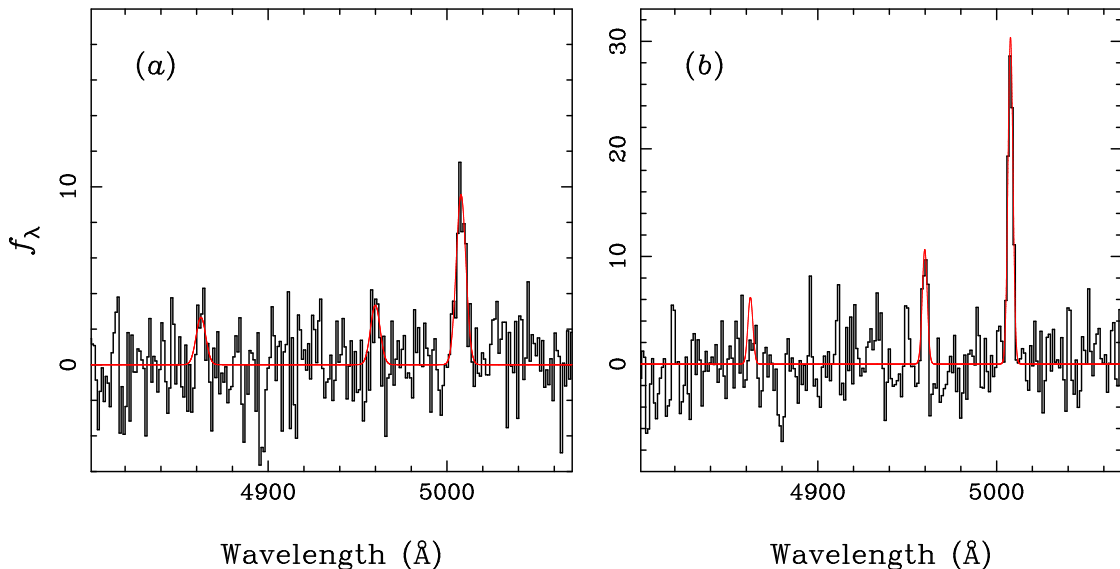


Fig. 3.—Determination of H β upper limits for two weak-lined objects, (a) J0932+3141 and (b) J1538+1204. Overlaid on each continuum-subtracted spectrum is an emission-line model consisting of the best-fit Gaussian to the [O III] $\lambda 5007$ line, the [O III] $\lambda 4959$ line expected from the $\lambda 5007$ fit, and the measured 3σ upper limit of H β , which is assumed to have the same velocity width as [O III]. In both cases, the model accurately represents the flux observed at $\lambda 4959$. Some H β flux appears to be present in the spectrum of J0932+3141, though the line is not formally detected.

In addition, we estimated lower limits on the combined [S II] $\lambda 6716 + \lambda 6731$ flux for potential AGN candidates in which the former line was detected but the latter line was not. A lower limit on their sum was obtained by assuming $F(\lambda 6716)/F(\lambda 6731) = 1.4$, which is the maximum ratio expected in low-density photoionized nebulae (Osterbrock 1989).

5. Results

5.1. Identifying AGNs in Low-Mass Galaxies

We used the following approach to construct our sample of AGNs in low-mass galaxies: (1) we culled all objects that, based on the available emission-line evidence, appear to be AGNs, (2) we verified the accuracy of the distances and photometry for all AGN candidates, and (3) we imposed a maximum value for the stellar mass of the AGN hosts.

Classification of the nuclear activity of the galaxies was made primarily on the basis of their locations on standard flux-ratio diagnostic diagrams, i.e., [O III] $\lambda 5007/\text{H}\beta$ vs. [N II] $\lambda 6583/\text{H}\alpha$, [O III] $\lambda 5007/\text{H}\beta$ vs. [S II] $\lambda\lambda 6716, 6731/\text{H}\alpha$, and [O III] $\lambda 5007/\text{H}\beta$ vs. [O I] $\lambda 6300/\text{H}\alpha$ (Veilleux & Osterbrock 1987). In most cases, we required that AGNs (a) lie across the empirical “maximum starburst line” (Kewley et al. 2006) from the locus of H II galaxies on each plot, and (b) have Seyfert levels of ionization with [O III] $\lambda 5007/\text{H}\beta$ ratios in excess of 3. Although LINERs and similar objects with [O III]/ $\text{H}\beta < 3$ can arise via photoionization by a dilute non-stellar continuum from an AGN (Ferland & Netzer 1983; Halpern & Steiner 1983; Filippenko & Halpern 1984; Ho et al. 2003), their observed line ratios can also result from purely stellar processes (Shields 1992; Filippenko & Terlevich 1992; Binette et al. 1994; Dopita & Sutherland 1995). Additionally, recent work has shown that even if an AGN is present, black-hole accretion is insufficient to power the emission lines associated with many LINERs (Eracleous et al. 2010; Yan & Blanton 2012). Thus, a LINER spectrum does not automatically point to the presence of a massive black hole, and we have excluded all LINER-like objects with low $\lambda 5007/\text{H}\beta$ ratios unless their spectra contain additional evidence in support of an AGN interpretation (e.g., high-ionization emission lines such as He II $\lambda 4686$, [Fe VII] $\lambda 6087$, and [Fe X] $\lambda 6375$, which are indicative of a hard ionizing continuum). In general, the high [O III]/ $\text{H}\beta$ condition set here ensures that the galaxies we select for further study are powered (at least in part) by black-hole accretion and that our sample, as a whole, is unconfused by non-AGNs — a prudent choice, given that the relationship between galaxies and black holes at low masses is not well understood.

For each AGN meeting the above criteria, we reexamined the estimated distance and SDSS photometry to select objects with stellar masses consistent with those of dwarf galaxies. Concerning distances, we searched the NASA/IPAC Extragalactic Database (NED) for objects with redshift-independent assessments of their distance (e.g., via the Tully-Fisher method), and we investigated whether objects presumed to be members of the Virgo cluster ($d \approx 14$ Mpc) might instead be background galaxies. As noted above in § 3, we used the DR7 Petrosian magnitudes for galaxies

whenever possible, adopting them if the associated aperture appears to collect all the light from an object and if there is good agreement between these measurements and the “model” magnitudes. For the majority of AGN hosts, the redshift-based distances and Petrosian magnitudes are indeed suitable. However, we identified a number of cases where it is likely that either the distance or brightness (and thus mass) has been underestimated, which caused us to remove several objects from our low-mass sample. A few objects with distance or photometry issues still qualify as dwarf galaxies when their stellar masses are revised; the problems and their remedies are described in § 5.5.

We corrected the *gri* magnitudes of the remaining low-mass AGN candidates for Galactic reddening (Schlafly & Finkbeiner 2011) and applied *K*-corrections using the methods of Chilingarian et al. (2010), which, for this low-redshift sample, typically affect only the value of *g*, and by at most a few hundredths of a magnitude. Also, since the emission lines of some objects have very high equivalent widths, we made adjustments to the galaxy magnitudes for the non-stellar flux from the active nucleus (details are provided in § 5.3.2). We then selected all AGNs whose host galaxies have stellar masses (via Bell et al. 2003) of $10^{10} M_{\odot}$ or less. The typical IMBH candidate discovered in previous SDSS surveys (e.g., Barth et al. 2008) resides in a galaxy with a stellar mass in excess of this value (see § 5.4).

In total, we have identified 28 dwarf galaxies with accreting central black holes. The SDSS images of the objects and their continuum-subtracted spectra in the $H\alpha$ and $H\beta$ regions are displayed in Figure 4. Table 1 lists the SDSS names, distance information, photometry data (which include the corrections discussed above), absolute *g* magnitudes, and stellar masses for the galaxies, along with any designations they may have in well-known catalogs (i.e., NGC, UGC, IC, etc.).

Table 2 contains emission-line data relevant to the classifications of the objects. In addition to the commonly reported line-flux ratios, we also include the $\text{He II } \lambda 4686/H\beta$ ratio for those with detected He II emission. The locations of our dwarf galaxy AGNs on the diagnostic flux-ratio diagrams are shown in Figure 5. Their positions with respect to the “maximum starburst” lines of Kewley et al. (2006) indicate that all, with two exceptions (see below), are clearly Seyfert nuclei. Only those objects with firm evidence of broad Balmer-line emission are classified as type 1 Seyferts in Table 2; the remainder are listed as Seyfert 2s. The classifications of the two objects denoted as “Sy2:” in the Table are less certain than the others; their emission lines are weak and the *S/N* ratios of their raw spectra are modest. They pass all of our tests, but should be confirmed as Seyferts with better data.

Two objects we have classified as Seyfert 2s do not quite meet the AGN criteria outlined above. The first, J0948+0958, has a high *S/N* ratio spectrum with line ratios that place it just inside the H II galaxy region on the $[\text{N II}]/H\alpha$ plot in Figure 5. However, it is well separated from the locus of star-forming galaxies shown, and in terms of its $[\text{S II}]/H\alpha$ and $[\text{O I}]/H\alpha$ ratios, the object resides comfortably amongst the other dwarf-galaxy AGNs in our sample. Moreover, it has a strong He II $\lambda 4686$ line (ionization potential = 54 eV). Depending on whether the He II profile is constrained to

have the same velocity width as the Balmer lines or is premitted to be broader (which results in a better fit), a $\text{He II}/\text{H}\beta$ ratio of 0.10–0.15 is indicated. This is close to the values expected for AGNs (e.g., Ferland & Netzer 1983) and far greater than those observed for pure star-forming galaxies in our sample, which have $\text{He II}/\text{H}\beta$ ratios of ~ 0.02 or less.

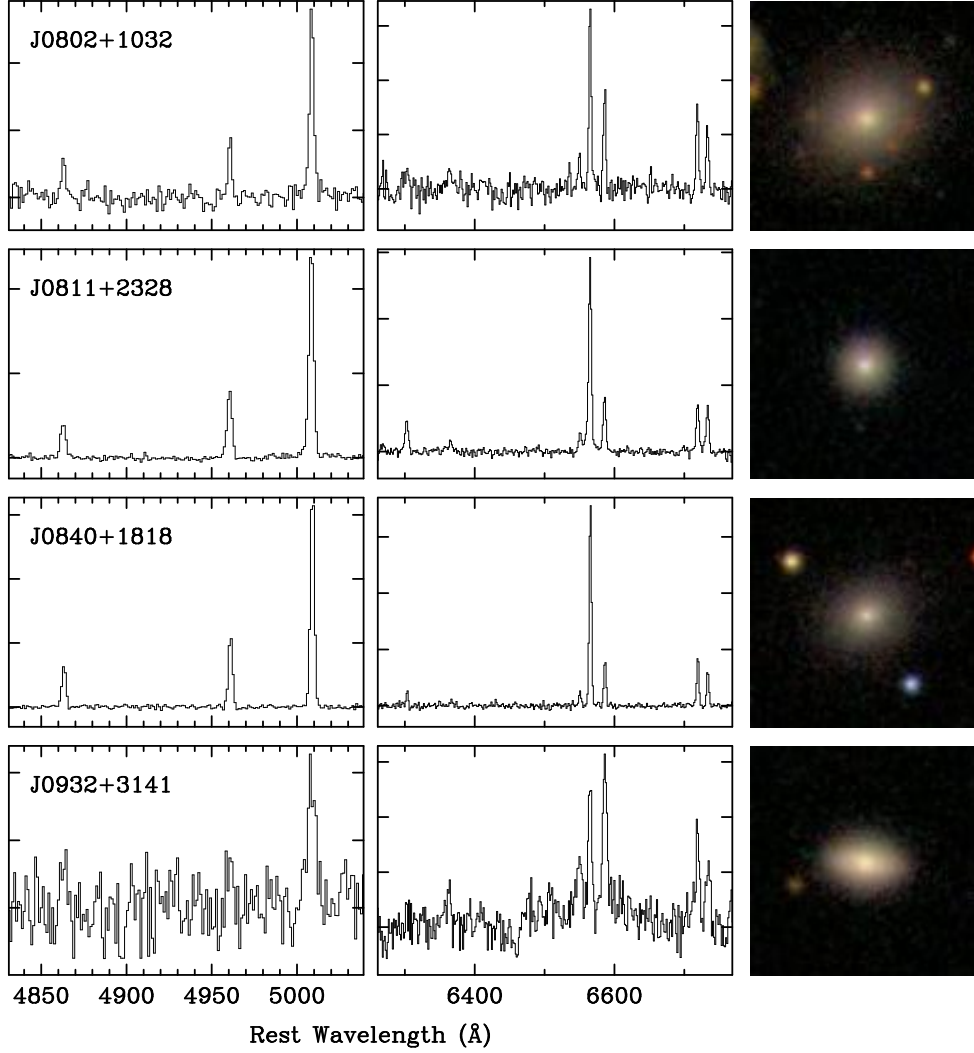


Fig. 4.—The dwarf-galaxy AGN sample. Displayed in the left and center panels are the continuum-subtracted spectra in the $\text{H}\beta$ and $\text{H}\alpha$ regions (the latter includes the $[\text{O I}] \lambda 6300$ line). The SDSS images of the objects, which have a physical scale of $12 \text{ kpc} \times 12 \text{ kpc}$, are shown on the right.

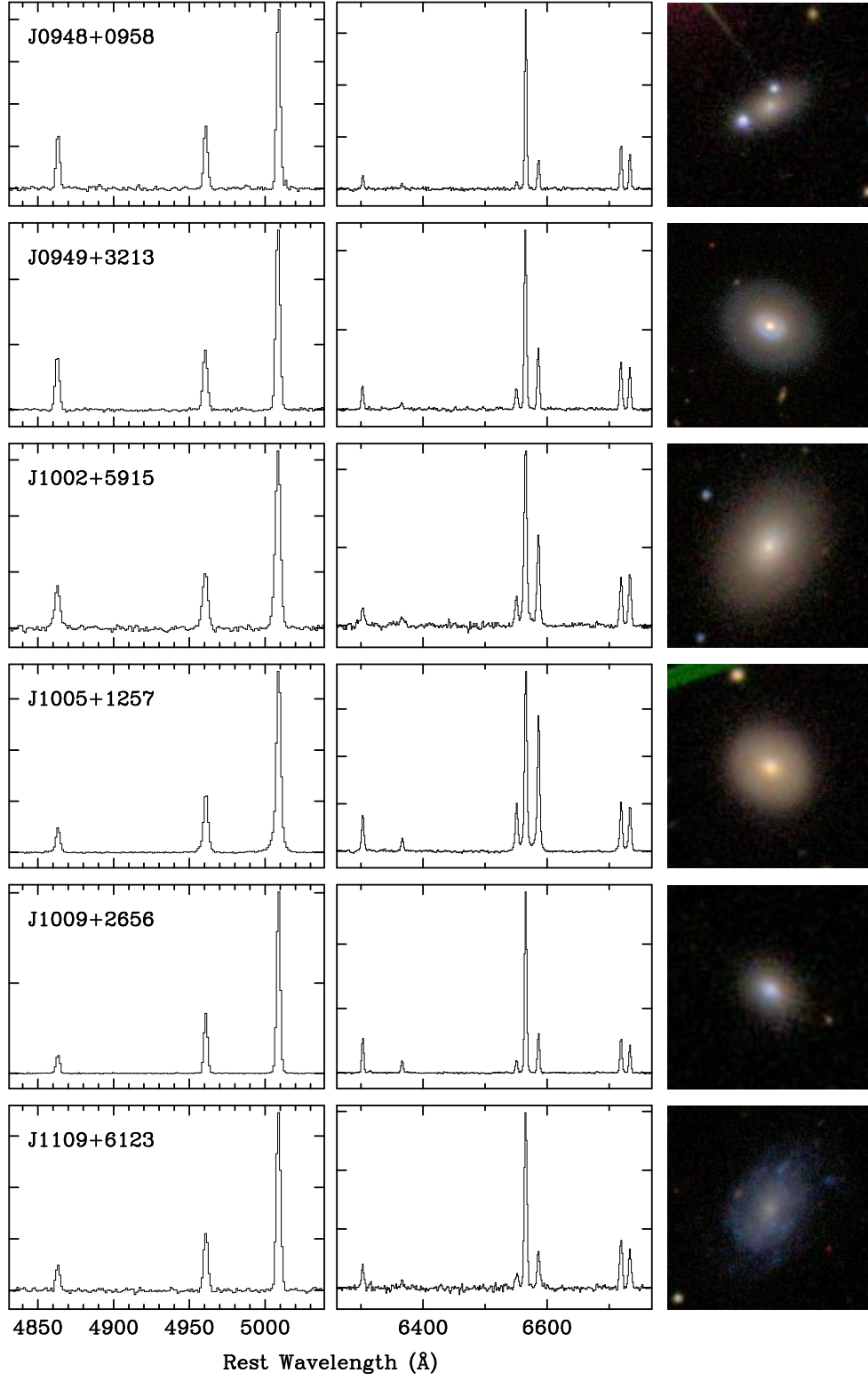


Fig. 4.—*continued*

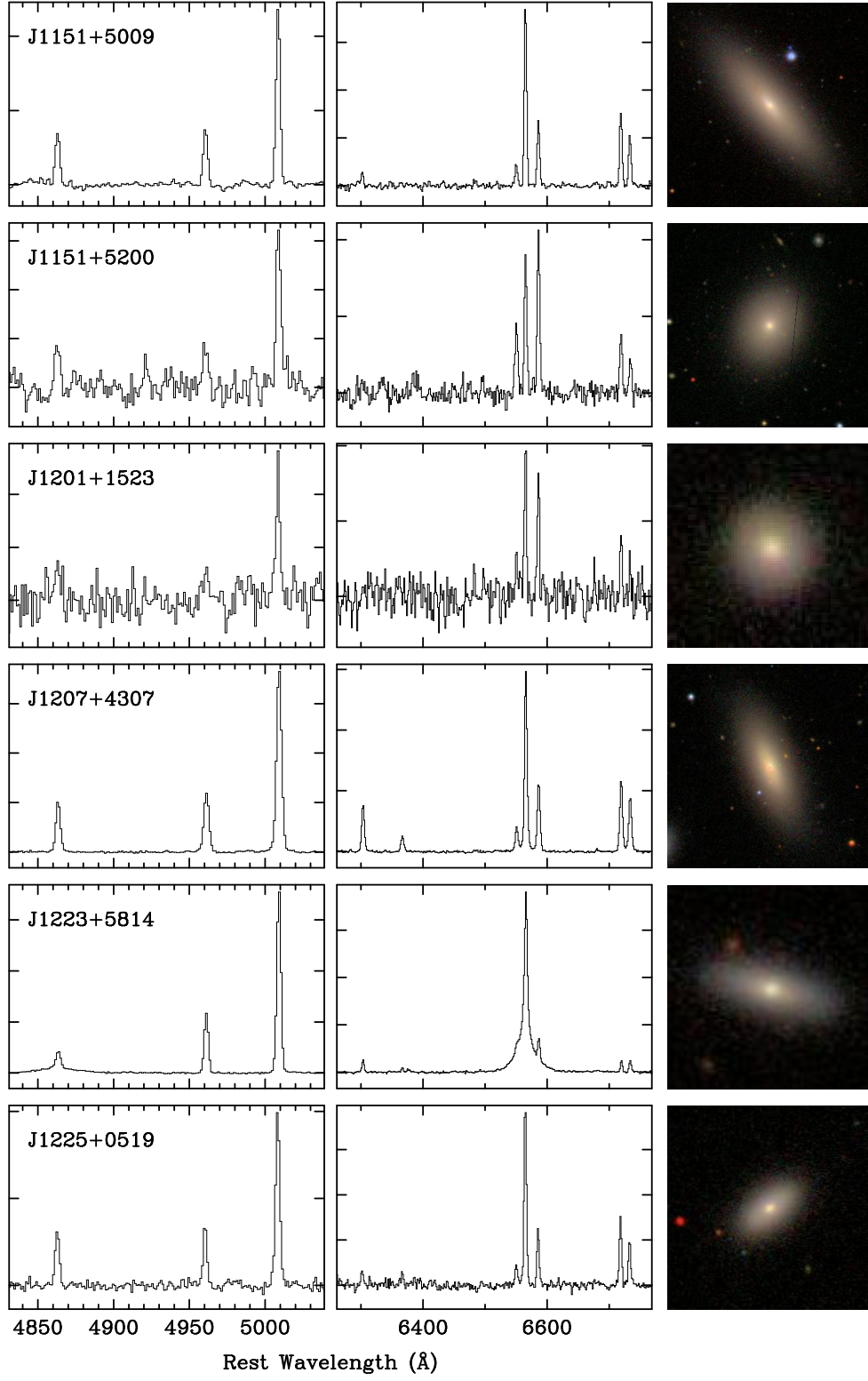


Fig. 4.—*continued*

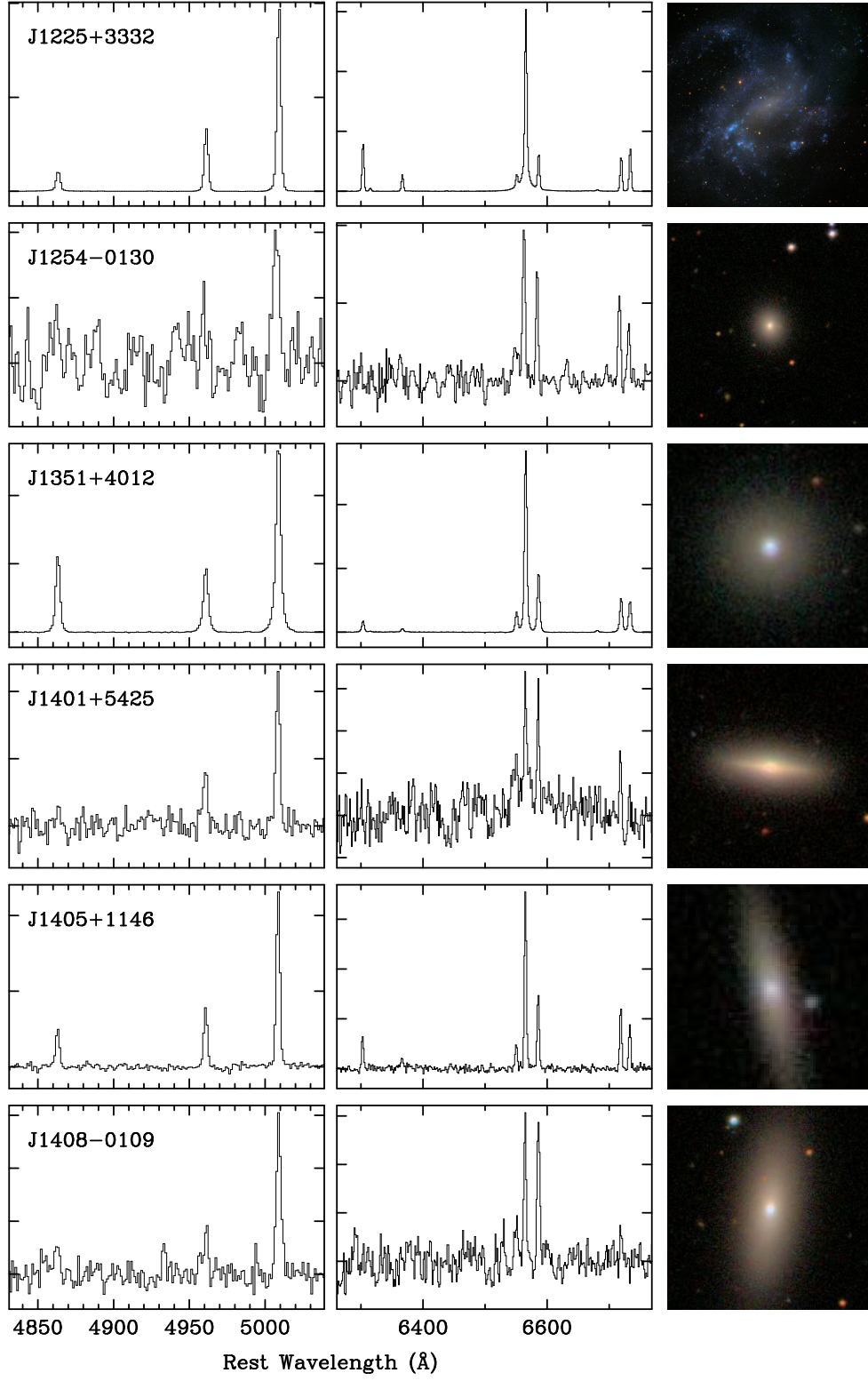


Fig. 4.—*continued*

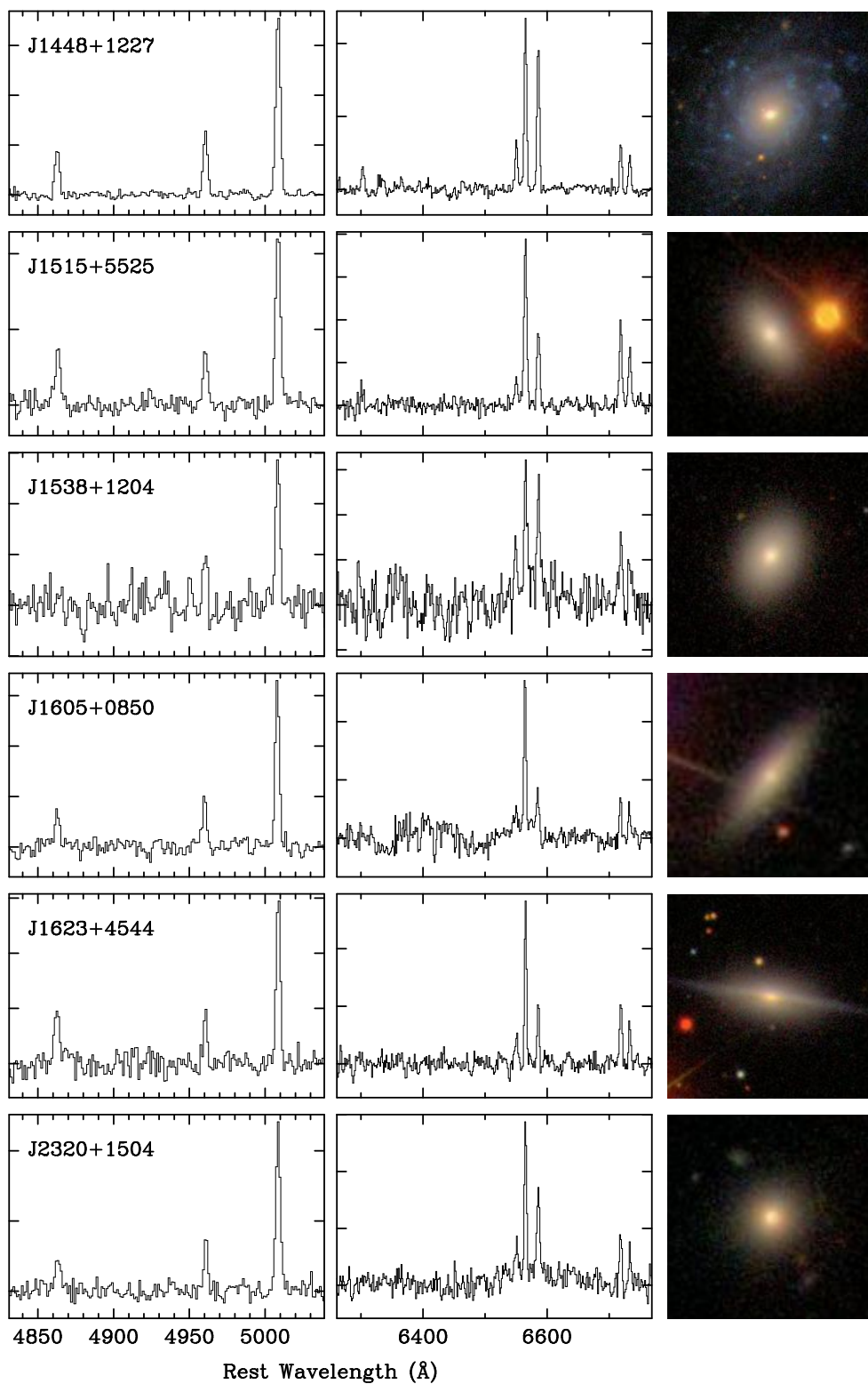


Fig. 4.—*continued*

Table 1. Galaxy Properties

SDSS Name	cz (km s ⁻¹)	d (Mpc)	g (mag)	$g - r$ (mag)	i (mag)	M_g (mag)	$M_*/10^9 M_\odot$	Catalog Names
J080212.06+103234.1	4358	62.2	16.10	0.66	15.06	-17.87	6.5	...
J081145.29+232825.7	4729	67.4	16.91	0.58	16.03	-17.23	2.7	...
J084025.54+181858.9	4483	64.9	16.84	0.61	15.95	-17.22	2.8	...
J093251.11+314145.0	4595	67.2	16.07	0.68	15.04	-18.07	8.1	...
J094800.79+095815.4 ^a	3110	47.3	16.51	0.48	15.73	-16.87	1.4	...
J094941.20+321315.9	1537	26.2	14.10	0.57	13.24	-17.99	5.1	NGC 3011, Mrk 409
J100200.96+591508.3	2805	43.2	14.72	0.60	13.78	-18.45	9.1	MCG +10.15.001
J100551.19+125740.6	2801	43.3	14.93	0.67	13.89	-18.25	9.4	IRAS F10031+1312
J100935.66+265648.9	4302	64.1	16.87	0.48	16.14	-17.16	1.8	...
J110912.39+612346.6	2014	33.3	15.46	0.27	15.14	-17.15	0.8	UGC 6192
J115113.43+500924.8	935	18.7	13.32	0.67	12.30	-18.03	7.6	NGC 3922
J115113.45+520003.0	905	18.2	13.87	0.67	12.86	-17.43	4.3	NGC 3931
J120108.03+152353.6	5176	78.4	16.07	0.65	15.09	-18.40	9.9	...
J120746.11+430734.8	934	18.5	13.61	0.76	12.47	-17.73	7.6	NGC 4117
J122342.81+581446.2	4355	65.3	16.05	0.60	15.12	-18.02	6.0	...
J122505.60+051944.7	2000	33.4	15.22	0.65	14.23	-17.40	4.0	...
J122548.86+333248.7 ^b	312	4.3	10.58	0.45	9.98	-17.28	1.1	NGC 4395
J125401.88-013030.0	1136	19.0	15.18	0.66	14.19	-16.22	1.3	...
J135125.37+401247.8	2465	41.3	15.02	0.58	14.18	-18.06	5.5	Mrk 462
J140116.03+542507.5	1893	33.0	14.44	0.72	13.33	-18.16	10.0	MCG +09.23.005
J140510.39+114616.9	5235	80.6	16.40	0.52	15.62	-18.13	5.0	IC 976
J140843.28-010941.9	1532	26.0	13.41	0.55	12.56	-18.67	9.2	UGC 9040
J144842.57+122725.9	1798	31.6	13.90	0.55	13.07	-18.60	8.4	NGC 5762
J151500.96+552555.2	3179	50.1	15.40	0.65	14.28	-18.10	8.4	...
J153851.70+120450.2	1992	34.3	14.27	0.64	13.29	-18.41	9.7	IC 1131
J160544.57+085043.9 ^c	4661	72.2	16.66	0.69	15.47	-17.63	6.4	...
J162335.07+454443.4	1858	32.6	14.87	0.67	13.83	-17.69	5.7	UGC 10370
J232028.21+150420.9	3843	52.9	15.75	0.67	14.72	-17.87	6.6	...

^aDR7 model magnitudes are listed.^bValues listed in the g , $g - r$, and i columns for this object are its B , $B - V$, and K magnitudes from the RC3 and 2MASS catalogs. The absolute g magnitude is estimated from these using the Lupton transformations (see § 5.5). The stellar mass is calculated via the BV/K magnitudes and the appropriate coefficients from Bell et al. (2003).^cDR8 Petrosian magnitudes are listed.

Table 2. Narrow Emission-Line Properties

Object	Class	He II/H β	[O III]/H β	[O III]/H α	[N II]/H α	[S II]/H α	[O I]/H α	$\log L_{5007}/L_{\odot}^a$	$\log M_{\text{BH,min}}/M_{\odot}$
J080212.06+103234.1	Sy2	...	5.12	0.53	0.81	5.09	3.6
J081145.29+232825.7	Sy2	...	6.06	0.24	0.44	0.15	0.15	5.91	4.4
J084025.54+181858.9	Sy2	0.13	5.35	0.22	0.41	0.07	0.07	5.87	4.3
J093251.11+314145.0	Sy2:	...	> 3.16	1.32	1.36	4.99	3.5
J094800.79+095815.4	Sy2	0.10	3.42	0.16	0.44	0.07	0.07	5.73	4.2
J094941.20+321315.9	Sy2	0.17	3.47	0.36	0.53	0.13	0.13	5.66	4.1
J100200.96+591508.3	Sy2	...	4.14	0.41	0.46	0.13	0.13	5.63	4.1
J100551.19+125740.6	Sy2	0.21	8.49	0.76	0.51	0.19	0.19	6.29	4.8
J100935.66+265648.9	Sy2	0.27	9.15	0.22	0.34	0.19	0.19	6.63	5.1
J110912.39+612346.6	Sy2	0.23	7.15	0.21	0.49	0.12	0.12	5.34	3.8
J115113.43+500924.8	Sy2	0.14	3.17	0.36	0.69	0.06	0.06	4.99	3.5
J115113.45+520003.0	Sy2	...	3.92	1.24	0.72	4.16	2.6
J120108.03+152353.6	Sy2	...	3.42	0.78	> 0.68	4.98	3.4
J120746.11+430734.8	Sy2	0.05	3.11	0.39	0.68	0.25	0.25	5.56	4.0
J122342.81+581446.2	Sy1	0.08	9.23	0.19	0.18	0.09	0.09	6.53	5.0
J122505.60+051944.7	Sy2	0.19	3.15	0.29	0.59	0.08	0.08	5.12	3.6
J122548.86+333248.7	Sy1	0.24	9.76	0.22	0.48	0.30	0.30	5.31	3.8
J125401.88-013030.0	Sy2:	...	> 3.12	0.65	0.92	3.81	2.3
J135125.37+401247.8	Sy2	0.08	2.92	0.32	0.36	0.06	0.06	6.54	5.0
J140116.03+542507.5	Sy2	...	> 7.30	0.87	> 0.92	4.74	3.2
J140510.39+114616.9	Sy2	0.16	4.55	0.43	0.60	0.18	0.18	5.90	4.4
J140843.28-010941.9	Sy2	...	5.28	1.06	> 0.37	4.75	3.2
J144842.57+122725.9	Sy2	...	4.12	0.85	0.47	0.14	0.14	5.39	3.9
J151500.96+552555.2	Sy2	0.26	3.02	0.45	0.82	0.12	0.12	5.20	3.7
J153851.70+120450.2	Sy2	...	> 5.00	0.79	> 1.03	4.65	3.1
J160544.57+085043.9	Sy2	...	4.20	0.35	0.44	5.33	3.8
J162335.07+454443.4	Sy2	...	3.03	0.38	0.67	4.55	3.0
J232028.21+150420.9	Sy2	...	4.69	0.61	0.60	5.25	3.7

^a $L_{\odot} = 3.8 \times 10^{33} \text{ ergs s}^{-1}$.

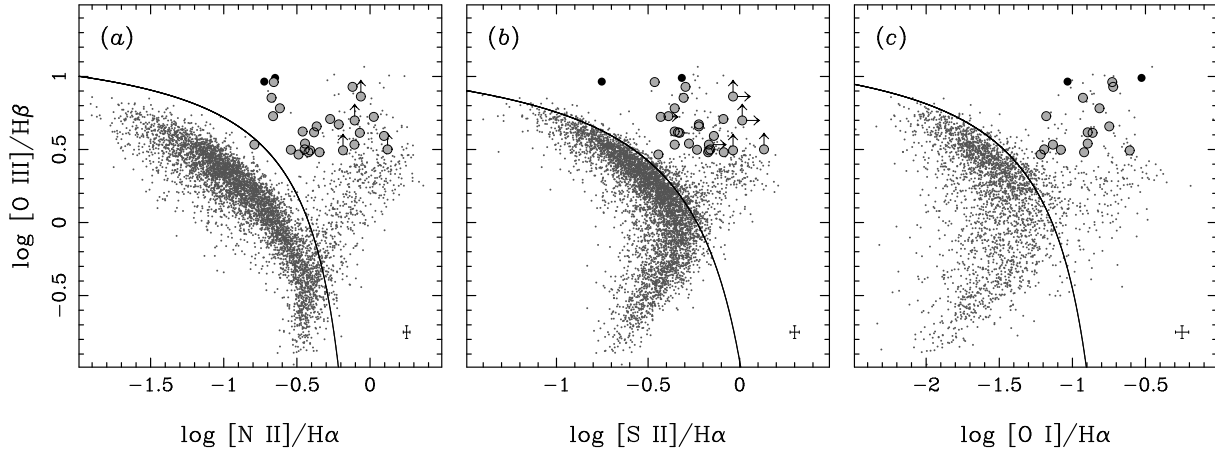


Fig. 5.—Locations of the dwarf-galaxy AGNs in our sample (circles) on standard emission-line diagnostic diagrams. Solid symbols represent the two objects with clear detections of broad emission lines. Lower limits on the $[\text{O III}]/\text{H}\beta$ and $[\text{S II}]/\text{H}\alpha$ ratios are indicated with arrows. Typical error bars, computed for the object in the sample that has the median S/N ratio for all detected diagnostic lines, are shown in the lower-right corner of each panel. The grey dots represent all SDSS DR7 galaxies within 80 Mpc that have detections of the relevant emission lines (5345 in the $[\text{N II}]$ and $[\text{S II}]$ plots, and 2826 in the $[\text{O I}]$ plot). Empirical “maximum starburst” lines (Kewley et al. 2006) separate the AGN and H II galaxy regions on the plots.

The second object, J1351+4012, lies in the AGN regions on all of the plots in Figure 5, but it has relatively weak low-ionization forbidden lines and $[\text{O III}]/\text{H}\beta < 3$ (although, because the $[\text{O III}]$ lines are broader than $\text{H}\beta$, the ratio is closer to 3 than the spectrum in Fig. 4 might suggest). Similar to J0948+0958, this object also has a fairly strong He II line with $\text{He II}/\text{H}\beta = 0.08$. Weak $[\text{Fe VII}] \lambda 6087$ and $[\text{Fe X}] \lambda 6375$ lines, both of which have ionization potentials in excess of 100 eV, appear to be present as well. The spectra of J0948+0958 and J1351+4012 near He II $\lambda 4686$ are displayed in Figure 6.

The combination of strong He II emission and the fact that some of the flux ratios involving low-ionization lines are consistent with those of Seyfert nuclei suggests that these galaxies are powered in part by AGNs. Without the benefit of additional data, our best hypothesis is that they are composite objects whose SDSS spectra contain emission from both an active nucleus and circumnuclear star-forming regions. Relative to a pure AGN spectrum, we would expect either the $\text{H}\alpha$ or $\text{H}\beta$ emission line to be enhanced in this scenario, which would explain the ambiguous line ratios of the objects. Indeed, the central region of J1351+4012 is very blue (its “fiber” magnitudes measured in the same area covered by the spectroscopic fibers indicate $g - r = 0.39$) and its continuum spectrum exhibits strong Balmer absorption, confirming the presence of a young stellar population.¹ Similarly, J0948+0958 is one of our bluer objects ($g - r = 0.48$). Being low-mass

¹J1351+4012 would also qualify as “composite” according to Kewley et al. (2006), owing to the fact that it falls

galaxies, J0948+0958 and J1351+4012 are valuable additions to our AGN sample. They also suggest new ways of identifying active black holes in star-forming dwarf galaxies.

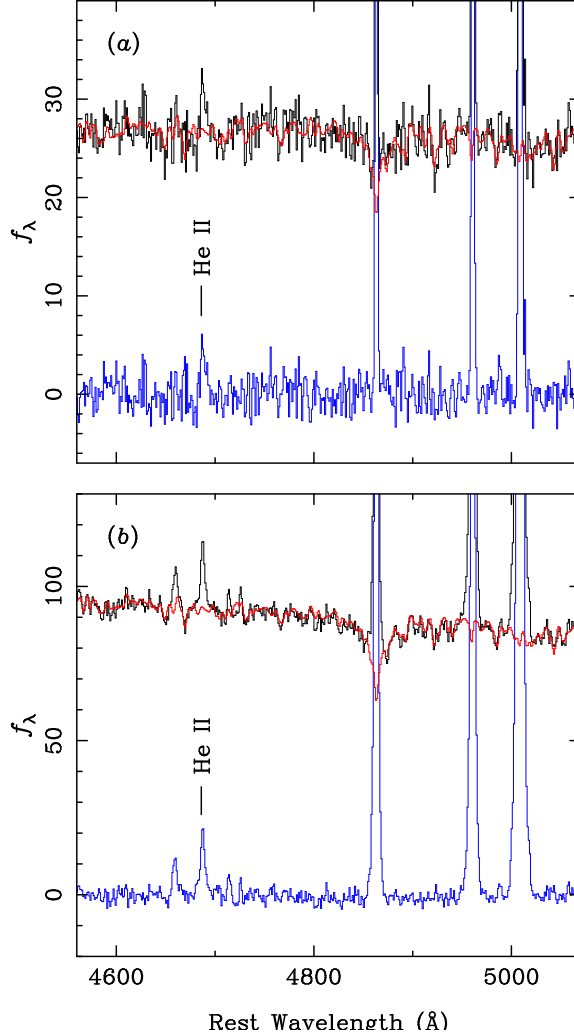


Fig. 6.—SDSS spectrum (black), continuum fit (red), and emission-line residuals (blue) in the vicinity of He II $\lambda 4686$ for (a) J0948+0958 and (b) J1351+4012, the two objects in our sample with ambiguous classifications. Although the narrow-line flux ratios of these objects do not strictly satisfy the Seyfert criteria we have adopted, the strength of the He II line (relative to $H\beta$) in each is typical of that observed in AGNs. In J1351+4012, He II is flanked by [Ar IV] $\lambda 4712$ to the red and what appears to be [Fe III] $\lambda 4658$ to the blue.

between the empirical and theoretical (Kewley et al. 2001) maximum starburst lines on the [O III]/ $H\beta$ vs. [N II]/ $H\alpha$ diagram. We note, however, that the one other object in our sample that would be composite by this definition, J1225+0519, displays no evidence of ongoing or recent star formation. It is very red (in terms of both its total and fiber magnitudes) and its nuclear spectrum is dominated by an old stellar population.

5.2. Nuclear Properties

The nuclear emission-line characteristics of the galaxies in our sample have played a primary role in their identification as AGNs. Bearing in mind that the continuum-subtracted spectra have a wide range of line strengths and S/N ratios, we have examined these characteristics more closely to gain additional insight into the nature of the objects.

5.2.1. Narrow Emission Lines

The narrow emission lines of AGNs contain information about the continuum source and the properties of the associated photoionized gas. Following Ludwig et al. (2012), who examined a subset of type 1 IMBH candidates from the SDSS surveys of Greene & Ho (2004, 2007b), we have measured the narrow He II $\lambda 4686/H\beta$ flux ratios for our objects when possible. This ratio provides an estimate of the slope of the ionizing continuum in the far-ultraviolet (Penston & Fosbury 1978) and an opportunity to compare the AGNs uncovered in our survey with existing samples of IMBH candidates. As Table 2 indicates, He II/ $H\beta$ = 0.05–0.27 for the 14 objects with a detected He II line. Assuming the UV continuum between 228 Å and 912 Å can be described as a power law (i.e., $F_\nu \propto \nu^{-\alpha_{UV}}$), this translates to a spectral index range of $\alpha_{UV} = 1.5$ –2.6, with a median value of 1.8. This distribution of power-law slopes is very similar to that obtained by Ludwig et al. (2012), suggesting that there are no significant differences in the ionizing continua of their more luminous broad-line objects and the predominantly narrow-line AGNs in our sample.

Weak [O III] $\lambda 4363$ emission is detected in the spectra of a dozen members of our sample. The measured fluxes, along with those of the other [O III] lines, indicate temperature-sensitive $F(\lambda 4959 + \lambda 5007)/F(\lambda 4363)$ ratios of ~ 40 –80, which correspond to electron temperatures of $T_e \approx (1.4 - 2.0) \times 10^4$ K in the narrow-line region (NLR) gas (Osterbrock 1989). Although some of the objects lacking $\lambda 4363$ detections could have lower temperatures (say, $\sim 10^4$ K), the median value for those with detections ($T_e \approx 1.5 \times 10^4$ K, based on a flux ratio of 63) is likely to be representative of the sample as a whole.

Assuming the [O III] and [S II] lines are produced in the same regions,² we can estimate the electron densities in the NLRs of our objects by combining this temperature and the density-sensitive [S II] $F(\lambda 6716)/F(\lambda 6731)$ flux ratio. Most of the AGNs in our sample have [S II] ratios that are tightly clustered around a value of ~ 1.4 , indicating NLR densities near the low-density limit. In fact, 20/28 objects have $F(\lambda 6716)/F(\lambda 6731) \geq 1.2$, implying $n_e \leq 10^2 \text{ cm}^{-3}$ (Osterbrock 1989). The electron densities of the remaining 8 objects, with [S II] ratios between 0.8 and 1.1, are in the ~ 500 –1200 cm^{-3} range.

²This may not be a safe assumption if the NLRs of our objects have significant density or ionization stratification, which is observed in some (but not all) luminous AGNs (e.g., Filippenko & Halpern 1984; Veilleux 1991).

One of the most striking aspects of the spectra shown in Figure 4 is that some objects exhibit exceptionally low $[\text{N II}]/\text{H}\alpha$ ratios, with values in the vicinity of ~ 0.2 . As Table 2 indicates, about half of our galaxies have $[\text{N II}]/\text{H}\alpha \leq 0.4$ — lower than the ratios observed for the vast majority of objects classified as AGNs in large SDSS surveys (e.g., Kewley et al. 2006). Weak $[\text{N II}]$ Seyferts, which are also present in the IMBH samples of Barth et al. (2008) and Ludwig et al. (2012), are good candidates for objects that have lower metal abundances in their NLR gas compared to classical Seyfert nuclei (Groves et al. 2006). As the latter reside in massive galaxies, this might be expected based on the observed mass-metallicity relation in galaxies (e.g., Tremonti et al. 2004). However, the ionization parameter in the NLR — i.e., the ratio of the densities of ionizing photons and gas — affects the $[\text{N II}]$ strength as well (e.g., Ferland & Netzer 1983), implying that the density and geometry of the NLR are also important factors.

We have used the photoionization calculations performed by Ludwig et al. (2012, based on the models of Groves et al. 2004) to explore the effects of metallicity and ionization parameter in our sample, particularly for those objects with the lowest $[\text{N II}]/\text{H}\alpha$ ratios. In their Figure 6, Ludwig et al. (2012) present predictions of the $[\text{O III}]/\text{H}\beta$ and $[\text{N II}] \lambda\lambda 6548, 6583/\text{H}\alpha$ flux ratios for a range of metallicity and ionization parameter values. For a continuum slope of $\alpha_{\text{UV}} = 1.7$ and a density of $n_e = 100 \text{ cm}^{-3}$ or $n_e = 1000 \text{ cm}^{-3}$ — appropriate assumptions for our sample — the Ludwig et al. calculations indicate that 6/7 of our objects with $[\text{N II}]/\text{H}\alpha \approx 0.2$ are located in a region of high ionization parameter ($\log U \approx -1$) and solar (or slightly super-solar) metallicity. As discussed by Ludwig et al., the determination of absolute metallicities is difficult, but combining all of the available spectral evidence, our findings suggest that a high ionization parameter is mainly responsible for the weakness of $[\text{N II}]$ in these objects. We note, however, that the ambiguous line ratios of the seventh weak- $[\text{N II}]$ object, J0948+0958, might be explained (in part) by NLR gas with sub-solar abundances. We speculated above in § 5.1 that the SDSS spectrum of J0948+0958 may be a combination of emission from an AGN and circumnuclear H II regions, but the $[\text{O III}]/\text{H}\beta$ and $[\text{N II}]/\text{H}\alpha$ ratios of this galaxy are consistent with the $Z = 0.5 Z_\odot$ model calculations in the $\alpha_{\text{UV}} = 1.7$, $n_e = 100 \text{ cm}^{-3}$ plot shown in Figure 6 of Ludwig et al. Interestingly, AGN-like $[\text{S II}]/\text{H}\alpha$, $[\text{O I}]/\text{H}\alpha$, and $\text{He II}/\text{H}\beta$ flux ratios, which J0948+0958 displays, are also expected in this scenario (Groves et al. 2006). Spatially resolved spectra of this object would help clarify its nature; in any case, it represents the best candidate for a low-metallicity AGN in our sample.

5.2.2. Broad Emission Lines

Examination of Figure 4 reveals that there is a paucity of objects with obvious broad emission lines in our sample. In fact, there are just two: one is J1225+3332, which is NGC 4395 itself, and the other is J1223+5814, the only object in the Greene & Ho (2007b) IMBH survey that falls within the redshift and stellar-mass limits of our study. The broad $\text{H}\alpha$ components in both objects are fairly narrow ($< 1000 \text{ km s}^{-1}$ FWHM), and similar to the broad lines in other type 1 IMBH candidates (e.g., Greene & Ho 2004), their profiles have extended, Lorentzian-like wings.

Figure 4 indicates that two other AGNs in our sample, J0932+3141 and J2320+1504, have features in their residual spectra reminiscent of broad $H\alpha$ lines. Indeed, a reanalysis of the spectra with GANDALF results in an improved fit when a broad-line component is included. However, the putative broad-line signal in each is extremely weak in comparison to the flux-density level in the raw data and the noise in the residual spectrum. In both cases, the formal S/N ratio of the fitted broad lines is only ~ 2 . Two other galaxies, J1401+5425 and J1538+1204, may also have broad $H\alpha$ lines, but if so, the significance of the detections is even lower. Until better data indicate otherwise, we consider all four of these objects to be narrow-line AGNs.

The “noise” spectra (described above) of several AGNs in our sample exhibit significant positive residuals in the wings of $H\alpha$, which might point to the presence of a broad-line component. However, in *all* such cases, similar residuals are also associated with the strong forbidden lines in the spectrum (e.g., [O III]). Modeling the emission lines using non-Gaussian profiles (e.g., Voigt) with a single velocity width, we obtain good fits to the spectra without the need for extra broad Balmer components.

Taken at face value, the data in hand would suggest that broad-line AGNs are quite uncommon in local dwarf galaxies. Only 2/28 objects in our sample have clear evidence of broad emission lines, which is far less than one would expect based on the 1:3 or 1:4 ratios of type 1 to type 2 Seyferts obtained in previous optical surveys of luminous AGNs (e.g., Osterbrock & Shaw 1988; Maiolino & Rieke 1995). In terms of possible selection effects, we point out that the detection of faint, moderately broad Balmer lines associated with low-mass black holes could be challenging. To draw firm conclusions about the relative numbers of type 1 and type 2 AGNs in our sample, we would require spectra of uniformly high S/N ratio (and higher spectral resolution). Alternatively, if the unified AGN model (e.g., Antonucci 1993) is applicable to Seyfert nuclei in dwarf galaxies, we might expect our sample to be biased in favor of unobscured (and hence brighter) broad-line objects, and not the weak type 2 objects that dominate it. The apparently low type 1/type 2 ratio we observe could thus be a hint that the broad-line regions of AGNs in the least luminous, least massive systems are more likely to be obscured than those of classical Seyfert nuclei. This is an important issue that should be explored further.

5.2.3. *Black Hole Masses*

The kinematic information contained in broad emission lines provides the opportunity to estimate black hole masses in AGNs (Xiao et al. 2011, and references therein). Obviously, with such a small number of type 1 AGNs, there is little we can say about the black-hole masses of our objects. We can, however, use Eddington-luminosity arguments to estimate the minimum masses of their black holes (e.g., Barth et al. 2008). To do this, we take L_{5007} , the luminosity of the strong (and presumably isotropic) [O III] $\lambda 5007$ emission line, and compute the bolometric luminosity L_{bol} by applying a bolometric correction (e.g., Heckman et al. 2004). The minimum black-hole mass is obtained by assuming the source is radiating at its Eddington limit — i.e., that $L_{\text{bol}} = L_{\text{Edd}}$ and

$$L_{\text{Edd}} = 1.3 \times 10^{38} M_{\text{BH}}/M_{\odot} \text{ ergs s}^{-1}.$$

Included in Table 2 are the values of L_{5007} for the objects in our sample, corrected for Galactic extinction. While it is common to adopt the Heckman et al. (2004) ratio of $L_{\text{bol}}/L_{5007} \approx 3500$ for L_{bol} estimates, we have instead derived a bolometric correction using the sample of broad-line AGNs from the Greene & Ho (2007b) IMBH survey. These are closer analogs to the objects in our sample, and in addition to L_{5007} measurements, they have published values of M_{BH} and $L_{\text{bol}}/L_{\text{Edd}}$ that are independent of L_{5007} . In Figure 7a, we plot the distribution of L_{bol}/L_{5007} ratios for 174 AGNs in the main sample of Greene & Ho. Ignoring the few outliers at the very low end, the distribution has a median of $\log(L_{\text{bol}}/L_{5007}) = 3.0$ and an RMS scatter of 0.3 dex.

Minimum black-hole masses based on this bolometric correction for our objects are also listed in Table 2. The distribution, shown in Figure 7b, has a median of $M_{\text{BH,min}} = 6 \times 10^3 M_{\odot}$ and a scatter of a factor of 5. The highest values are $\sim 1 \times 10^5 M_{\odot}$.

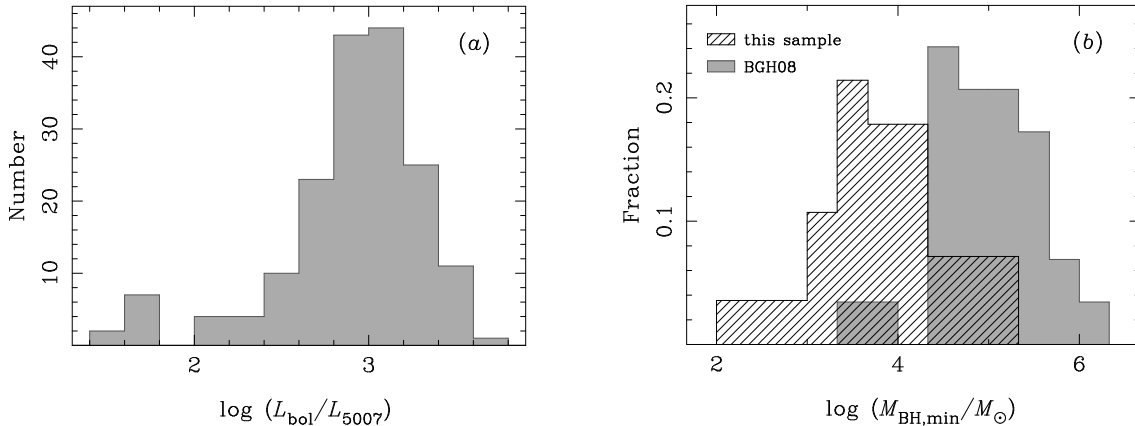


Fig. 7.—(a) Distribution of $\log(L_{\text{bol}}/L_{5007})$ values for the type 1 IMBH candidates in the main sample of Greene & Ho (2007b). Excluding the handful of outliers with extremely low ratios, the distribution has a median of 2.97 and an RMS scatter of 0.30 dex. (b) Distribution of minimum black-hole masses of the objects in our sample, derived using their measured L_{5007} values and the bolometric correction implied by the L_{bol}/L_{5007} distribution shown in (a). For comparison, we have included the minimum black-hole masses for objects in the IMBH sample of Barth et al. (2008, labeled “BGH08”), which is similar to ours in many respects. As described in § 5.4, we have taken care to eliminate systematic differences in the approach used to make the $M_{\text{BH,min}}$ estimates for the two samples.

The two type 1 AGNs in our sample, J1223+5814 and NGC 4395, have published black-hole masses of $\log(M_{\text{BH}}/M_{\odot}) = 6.05$ and 5.56, respectively, based on the width and luminosity of broad $\text{H}\alpha$ (for J1223+5814; Xiao et al. 2011) or the reverberation mapping technique (for NGC 4395; Peterson et al. 2005). The minimum black-hole masses we have computed imply reasonable Eddington ratios of $\log(L_{\text{bol}}/L_{\text{Edd}}) = -1.1$ for J1223+5814 and $\log(L_{\text{bol}}/L_{\text{Edd}}) = -1.8$ for NGC 4395. The value for NGC 4395 is consistent with the recent $L_{\text{bol}}/L_{\text{Edd}}$ estimate by Nardini & Risaliti (2011).

5.2.4. Previous AGN Identifications and Non-Optical Detections

Despite their proximity, only four of the objects in our sample are previously classified AGNs. In addition to NGC 4395 and J1223+5814, our sample includes J1207+4307 (= NGC 4117), which has been part of numerous surveys of Seyfert galaxies over the years (e.g., Ulvestad & Wilson 1989; Cardamone et al. 2007), but it has not been recognized as an IMBH candidate in a low-mass host galaxy. The other known AGN is J1109+6123, a low-mass spiral galaxy that was included in the IMBH survey of Barth et al. (2008) and examined in detail by Thornton et al. (2009). All remaining 24 objects in our sample are newly classified AGNs, and many of these — other than having “galaxy” designations in the SDSS or the Two Micron All-Sky Survey (2MASS; Skrutskie et al. 2006) — are anonymous. Among the half-dozen “named” objects, a few have been classified in the literature as H II galaxies; they are discussed further in § 5.5.

It is also interesting to note that very few of the objects in our sample have been detected via emission that can be associated with black-hole accretion in bands other than the optical. Both NGC 4395 and NGC 4117 — two of the nearest objects — have been studied at X-ray wavelengths (e.g., Moran et al. 1999; Cardamone et al. 2007), and J1223+5814 was detected in the *ROSAT* All-Sky Survey (Mickaelian et al. 2006). One other object, J1515+5525, was marginally detected as a serendipitous source in a 27 ks observation with the ACIS-S instrument on board *Chandra*. We have just carried out *Chandra* observations of six additional AGNs in our sample and can report that very few counts were detected for any of them, even though the exposures were fairly deep (full details will be provided elsewhere). The situation in the radio band is similar. A search of the *FIRST* survey catalog (Becker et al. 1995) reveals that only three of the 27 objects observed are detected at 20 cm: NGC 4117 (1.9 mJy), NGC 4395 (1.2 mJy), and J1005+1257 (8.6 mJy).

The general weakness of our sample at radio and X-ray wavelengths is important in the context of how we construct samples of IMBH candidates. Recently, X-ray observations, either alone (e.g., Gallo et al. 2008; Desroches & Ho 2009; McAlpine et al. 2011; Secrest et al. 2012; Araya Salvo et al. 2012; Schramm et al. 2013) or in combination with radio observations (Reines et al. 2011), have been used to identify a small number of IMBH candidates. While it remains to be seen if accreting IMBHs best express themselves as emission-line objects or as sources in the X-ray and radio bands, the size and properties of our sample suggest that, at least locally, optical techniques may provide the most economical means for discovering low-luminosity (and potentially the most typical) examples.

5.3. Host Galaxy Properties

5.3.1. Sizes, Morphologies, and Environments

The broadband SDSS images of the AGN host galaxies in our sample are shown at a common scale of $12 \text{ kpc} \times 12 \text{ kpc}$ in Figure 4, demonstrating that the objects are indeed physically small.

Several of the galaxies have total diameters of less than 6 kpc. Figure 4 also indicates that all of the galaxies have regular morphologies with bright, compact knots at their centers. But with the exception of NGC 4395 (see § 5.5), the continuum emission in the spectra of our objects is dominated by starlight, implying that most of the light from these knots is associated with the galaxies’ central stellar concentrations, not their active nuclei. Interestingly, the images also reveal that only 3/28 galaxies are obvious spirals with blue, star-forming disks. Most of the rest have a smooth, featureless appearance (and often reddish colors) outside the nucleus, which might suggest that they are early-type galaxies. However, many of the latter objects have high axis ratios (e.g., J1151+5009, J1207+4307, J1223+5814, J1225+0519, J1405+1146, J1408–0109, and J1605+0850) and must be inclined disks rather than elliptical galaxies. Those with axis ratios close to unity could be more face-on versions of these galaxies. At least one object, though — J1623+4544 — appears to be an edge-on S0 galaxy with a significant spheroidal component. A detailed characterization of the central regions of the objects in our sample would provide valuable information about the stellar environments of their black holes (masses, luminosities, and surface brightness profiles; see Greene et al. 2008). Unfortunately, given the distances to some of the galaxies and the typical seeing in SDSS images, higher resolution images are needed for this task.

Combining a visual inspection of the SDSS images with tools available from NED, we find that most of the objects in our sample are isolated. None of them is a close binary companion of a more massive galaxy, and with the exception of two objects, none has a companion of any sort that is at roughly the same redshift and within a projected distance of ~ 10 galaxy diameters (D_{gal}). One of the objects with a close companion is J1207+4307 (= NGC 4117), which lies within $\sim 1 D_{\text{gal}}$ of the dwarf star-forming galaxy NGC 4118 and $\sim 4.5 D_{\text{gal}}$ from the LINER NGC 4111. The other is J1223+5814, which is separated by $\sim 3 D_{\text{gal}}$ from a fainter galaxy at about the same redshift. Four other galaxies in our sample are found 10–12 D_{gal} from galaxies at similar infall-corrected distances: J1109+6123 (near NGC 3543), J1201+1504, J1515+5525 (near the Seyfert 1 NGC 5905), and J1538+1204 (near the LINER NGC 5970). The rest (21/28) appear to be field galaxies. Thus, for the majority of our sample, clear evidence for external triggers of their nuclear activity is lacking.

5.3.2. Colors, Stellar Populations, and Stellar Masses

As mentioned in § 5.1, we corrected the total magnitudes of the galaxies in our sample for any non-stellar emission associated with their active nuclei. To do this, we multiplied both the original spectrum and the residual spectrum by the SDSS filter transmission functions to determine the contribution of the emission lines to the *gri* fiber magnitudes.³ The AGN-corrected fiber magnitudes

³The spectral modeling results described in § 4 indicate that the continua of all but one of the objects in our dwarf galaxy AGN sample are dominated by starlight, so only the emission-line fluxes were accounted for in this analysis. The continuum of the one object with a significant power-law component, J1225+3332, appears to have *no* starlight

were then used to adjust the total magnitudes of each galaxy. In the end, this analysis had little effect on their magnitudes and colors — the most significant change involved J1009+2656, which became fainter in g by 0.04 mag and redder in $g - r$ by 0.02 mag.

With a median value of $g - r = 0.64$, the total colors of the galaxies in our sample tend to be fairly red, and most of the objects with red colors have nuclear spectra that are dominated by light from an old stellar population (as indicated by the dominant starlight templates used in the continuum fits). Only nine galaxies have nuclear spectra whose continua are associated with either an intermediate-age (e.g., J0811+2328, J0948+0958) or young (e.g., J1009+2656, J1351+4012, J1405+1146) stellar population. We note that most of the objects with the lowest $[\text{N II}]/\text{H}\alpha$ flux ratios are found amongst this group. The correspondence between the line ratios and central star-formation histories of the galaxies might suggest that nitrogen abundance is a factor. However, there are several counter-examples; J1223+5814, J1225+0519, and five other galaxies with low $[\text{N II}]/\text{H}\alpha$ ratios have continua dominated by cool stars, while J1408–0109, which has a very blue nuclear spectrum (fiber $g - r = 0.35$), has one of the highest $[\text{N II}]/\text{H}\alpha$ ratios in the sample.

Despite having a wide range of colors ($g - r = 0.27\text{--}0.76$) and absolute magnitudes ($M_g = -16.2$ to -18.7), the stellar masses of the AGN host galaxies occupy a fairly narrow range between $\sim 10^9 M_\odot$ and $10^{10} M_\odot$. There are a fair number of objects (9/28) above $M_\star = 8 \times 10^9 M_\odot$, consistent with the increase in the numbers of AGNs with increasing stellar mass that we observe in the full SDSS sample. At lower masses, the M_\star distribution of the AGN hosts is fairly flat, but the cutoff at $\sim 10^9 M_\odot$ is abrupt. Incompleteness does affect the parent sample below $10^9 M_\odot$ (see Fig. 1), but there are well over 3000 galaxies in the $10^8 - 10^9 M_\odot$ range, so this cannot be the main reason for the sharp cutoff. The argument frequently given for the rarity of emission-line AGNs among blue late-type galaxies (e.g., Desroches & Ho 2009) is that such objects are likely to contain lower mass black holes and have enhanced levels of star formation. Thus, we might expect optical signatures of their nuclear activity to be relatively weak and more easily masked by the emission from circumnuclear H II regions. As Figure 8 shows, the full SDSS sample does get bluer with decreasing mass, so this scenario may indeed be relevant for our survey. On the other hand, some of the AGNs *are* located in blue, low-mass galaxies or in higher mass objects with blue central regions that exhibit evidence of recent star formation. As we discuss in § 5.4, our sample is less affected by luminosity bias than other samples, so the objects in it may better represent the population of dwarf galaxies with active nuclei. If so, the stellar masses and colors of the AGNs shown in Figure 8 might reflect (in part) the galaxy properties associated with the presence of a central black hole. A comparison of the morphologies of the AGN host galaxies with those of objects from the full SDSS sample with similar masses would complement the simple color analysis presented here.

in its spectrum, so we assigned all of the flux corresponding to the fiber magnitudes to the AGN in this case.

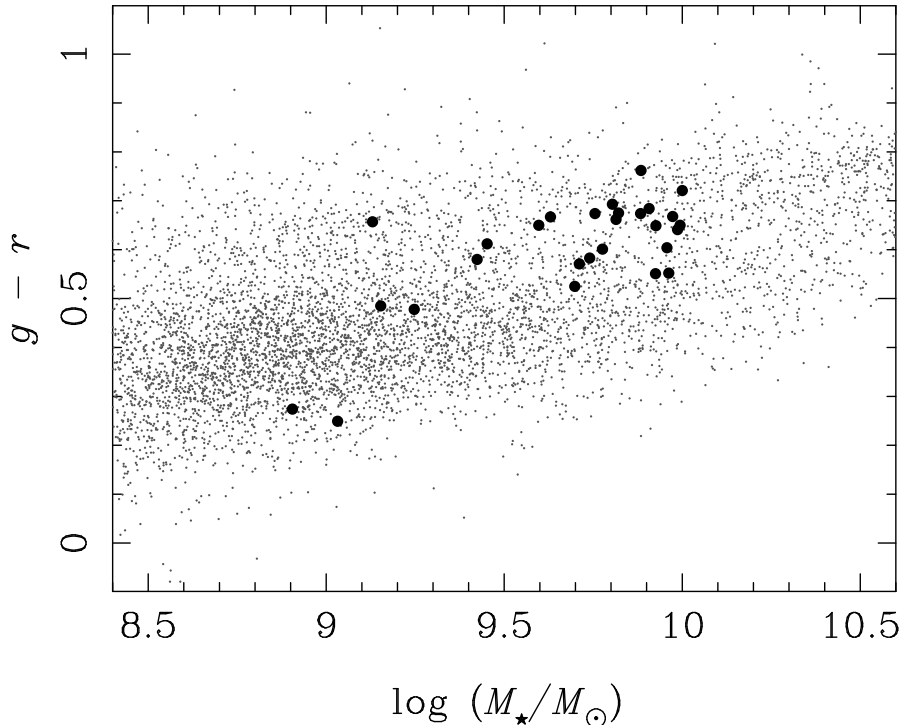


Fig. 8.—Total color vs. stellar mass for the full SDSS sample (grey dots), highlighting the AGNs we have identified (filled circles). Galaxies in the parent sample — as well as the AGN hosts — tend to get bluer with decreasing stellar mass.

5.4. Comparison to Other Searches for Low-Mass AGN Hosts

One way to assess the results of our survey and the effectiveness of our approach is to compare our sample of dwarf-galaxy AGNs to those of other SDSS-based IMBH surveys. Because of their focus on broad-line AGNs, the Greene & Ho (2007b) and Dong et al. (2012) surveys are not suitable for such a comparison. However, the Barth et al. (2008, hereafter BGH08) study is ideal in several respects. It, too, targeted low-mass AGN host galaxies, and as with our sample, most of the objects included in it (27/29) are narrow-line AGNs. Most importantly, BGH08 used essentially the same spectral classification criteria for identifying AGNs, and through detailed analysis of follow-up high-resolution spectra, they confirmed that all of the objects in their sample are powered by black-hole accretion. Statistically, the main difference between our surveys is in their data selection methods. To ensure that the comparison is as direct as possible, we have remeasured all quantities of interest for the BGH08 objects from the SDSS DR7 data in exactly the same manner as for our own sample, i.e., we determined distances and host-galaxy photometry the same way, measured emission-line fluxes from the continuum-subtracted SDSS spectra, and applied all of the various corrections described above. The values we obtain for absolute magnitude, stellar mass, and [O III] luminosity are thus similar, but not identical, to those listed in Table 1 of BGH08.

In terms of nuclear luminosity, we find that our sample is substantially fainter than that of BGH08. For our sample, $\log(L_{5007}/L_{\odot})$ has a median of 5.3 and a range of 3.8–6.6, whereas for BGH08 the median and range are 6.5 and 5.2–7.7, respectively. As a consequence, the distributions of minimum black-hole mass (which scales with L_{5007}) for the two samples differ significantly; see Figure 7b. This could reflect lower actual black-hole masses in our objects, lower average accretion rates, or some combination of the two. A comparison of the host galaxies is not as straightforward — stellar masses were computed differently for the BGH08 objects, and they set a different M_{\star} cutoff in their survey. Still, the AGN host galaxies in our sample tend to be fainter (median $M_g = -17.9$, compared to -18.9 for BGH08) and less massive (median $M_{\star} = 6 \times 10^9 M_{\odot}$ for our sample vs. $1.2 \times 10^{10} M_{\odot}$ for BGH08). Figure 9, which plots nuclear luminosity and host-galaxy mass, provides a concise summary of the differences between the samples. Overall, the lower values of L_{5007} and M_{\star} of our objects imply that our sample is less affected by luminosity bias, which is largely due to the lower distance limit we have adopted for our survey and the different approach we have used to select AGNs.

Contemporaneous with our work, Reines et al. (2013) have presented a sample of $z \leq 0.055$ IMBH candidates in low-mass host galaxies selected from the SDSS via the NASA-Sloan Atlas. A comparison between their results and ours is complicated by differences in the spectral classification criteria, e.g., they have included objects with $[\text{O III}]/\text{H}\beta < 3$, have segregated “composite” objects that fall between the empirical and theoretical maximum starburst lines on line-ratio plots (see Kewley et al. 2006), and have included a large number of objects that have H II region-like narrow-line ratios on one or more of the diagnostic diagrams. However, most ($\sim 32/35$) of the objects Reines et al. classify as “AGN” would be considered Seyferts using our criteria, and likewise, all but two or three of the 28 objects in our sample would qualify as “AGN” according to their criteria. Therefore, most of the comparisons that follow pertain to their “AGN” subsample.

The nuclear luminosities of the Reines et al. AGNs, computed from the redshifts and $[\text{O III}]$ fluxes listed in their tables, have a range of $\log(L_{5007}/L_{\odot}) = 5.2\text{--}7.7$ (the same as BGH08). Their median luminosity exceeds ours by a factor of 5. In fact, 12 of our objects have L_{5007} below that of the least luminous Reines et al. AGN. Thus, as with other SDSS surveys for IMBH candidates, the Reines et al. sample appears to be more affected by luminosity bias than ours. The reason our sample extends to lower luminosities is due in part to the fact that we have not imposed S/N ratio or equivalent width (EW) limits on any of the diagnostic emission lines, whereas Reines et al. required $S/N > 3$ and $\text{EW} > 1 \text{ \AA}$ for $\text{H}\alpha$, $[\text{O III}] \lambda 5007$, and $[\text{N II}] \lambda 6583$. Figure 10 illustrates how these limits would impact our sample. As shown in Figure 10a, all of our objects easily exceed the S/N ratio limit for $[\text{O III}] \lambda 5007$ set by Reines et al., but four of them would fail to meet their $[\text{O III}]$ EW requirement. As Figure 10b indicates, these four objects are among our least luminous AGNs. The situation is similar for $[\text{N II}] \lambda 6583$ — three additional low-luminosity AGNs in our sample that have sufficient S/N ratios would miss the Reines et al. EW cut for this line. Thus, it would appear that EW limits, when applied to AGNs that have otherwise well-detected lines, can

contribute to luminosity bias.⁴ Note, however, that five of the 12 objects in Figure 10b with L_{5007} below the Reines et al. minimum would meet all of the emission-line requirements for inclusion in their survey, so this is not the only reason the luminosity distributions of our AGN samples differ.

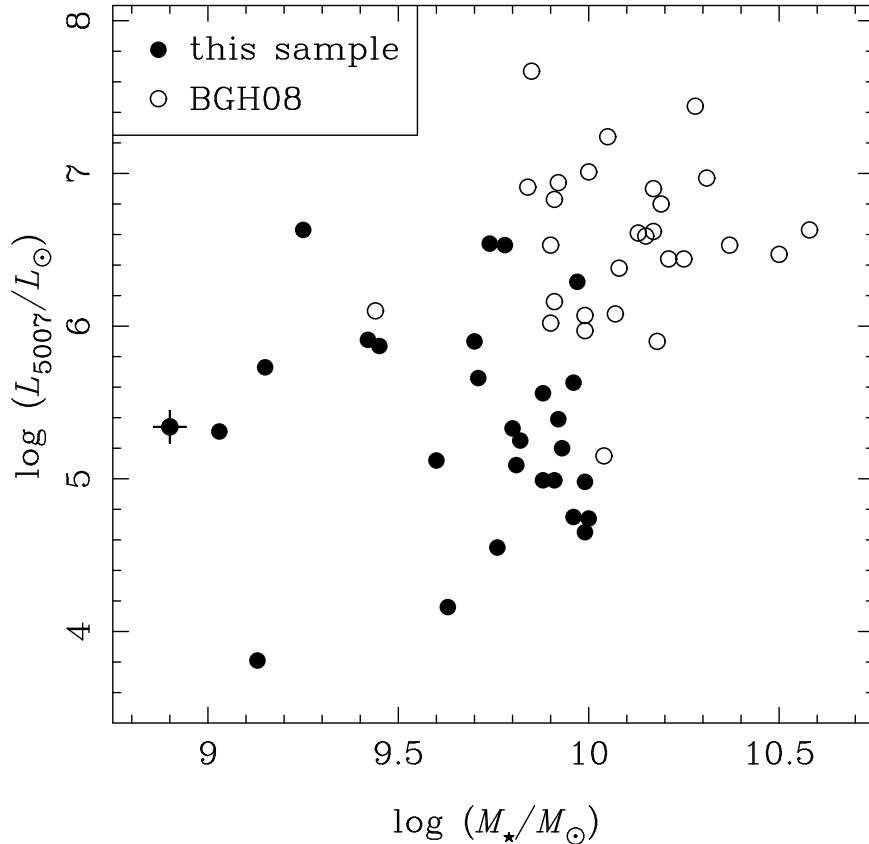


Fig. 9.—Summary of the differences in the nuclear luminosities (as indicated by L_{5007}) and stellar masses of the objects in our sample and that of BGH08. The filled circle superposed with a cross marks the one object common to both samples, J1109+6123. The generally lower values of L_{5007} and M_{\star} for our objects suggest that our sample is less affected by luminosity bias. The 1σ uncertainties in L_{5007} are of order the size of the symbols shown.

Considering stellar masses, Reines et al. intended to select objects with $M_{\star} \leq 3 \times 10^9 M_{\odot}$. However, it appears that the SED fitting technique used to compute their stellar masses yields systematically lower values of M_{\star} compared to the approach employed here. Applying our method to their sample (as we did for BGH08), we find that the stellar masses of two objects remain the

⁴Reines et al. also required $S/N > 2$ for $H\beta$. As discussed in § 4.3, four AGNs in our sample have $H\beta$ flux upper limits, and given that all four have low [O III] luminosities, one could argue that S/N ratio limits for $H\beta$ are also relevant for luminosity bias. However, these four objects are among the seven AGNs that would miss the Reines et al. EW cut for one of the other lines. Thus, the $H\beta$ S/N ratio limit adopted by Reines et al. would not by itself cause any low-luminosity objects to be excluded from our sample.

same, but those for the remainder of the sample all increase by factors of 1.5 to 8.3. The median increase is a factor of 2.4; stellar masses range up to $1.1 \times 10^{10} M_{\odot}$, and with one exception — J1109+6123, which is common to both samples and whose stellar mass is unchanged — none of the objects is less massive than $M_{\star} = 1.0 \times 10^9 M_{\odot}$. Four Reines et al. AGNs would be found in the lowest mass bin ($< 2 \times 10^9 M_{\odot}$), compared to 5/28 for our sample. This is by no means a statement about which method for calculating M_{\star} is more accurate — the point here is that there is essentially no contrast between our samples in terms their stellar mass distributions.

The full Reines et al. sample of IMBH candidates contains more galaxies than ours, partly because their survey covers a broader range of redshifts (80% of their “AGNs” lie beyond our distance limit⁵), but also because the requirements we have set to establish sample membership differ considerably. We estimate that no more than 36% of their full sample would meet the AGN selection criteria outlined in § 5.1. The types of objects in the Reines et al. sample that we have elected to omit in our survey are mainly (a) [N II]/H α “composite” galaxies that have [O III]/H β ratios well below 3, and (b) galaxies whose narrow-line flux ratios can be fully explained by star-forming activity.

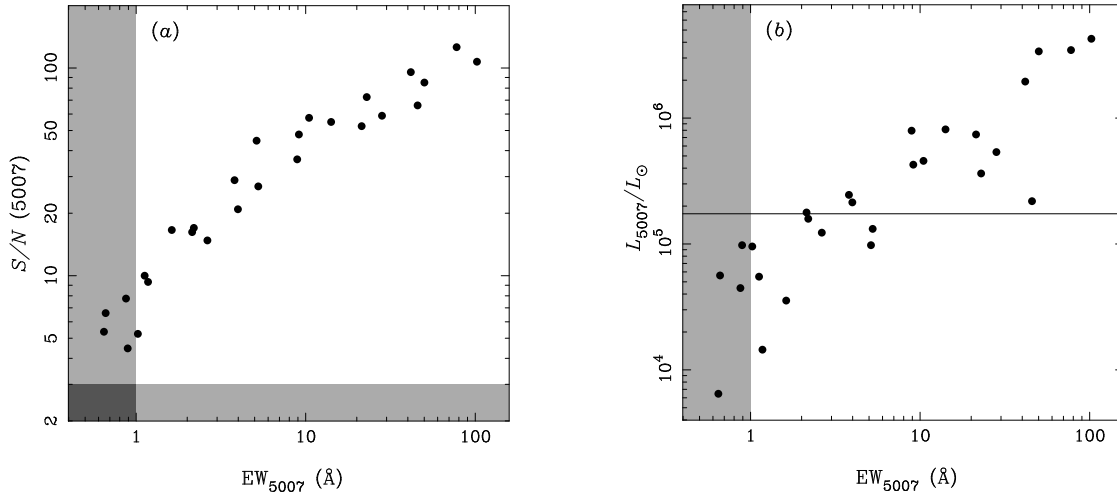


Fig. 10.—(a) The [O III] $\lambda 5007$ S/N ratios (computed by GANDALF in the full continuum fits) and equivalent widths (EWs) for our sample of AGNs. The shaded regions indicate the values excluded by Reines et al. (2013) in their search for AGNs in low-mass galaxies. Four of our objects would miss their EW cut, but all exceed the S/N ratio limit. (b) Comparison of the [O III] luminosities and EWs for our sample. Again, the shaded region represents EW values excluded by Reines et al. The horizontal line indicates the L_{5007} value of their least luminous AGN. Applied to our sample, the EW limit would remove some, but not all, low-luminosity nuclei. One object — NGC 4395 — has a very high EW_{5007} and is not included on either plot.

⁵In our redshift range, the samples have seven objects in common, and as discussed in § 5.2 and § 5.5, three of these — J1109+6123, J1223+5814, and NGC 4395 — are previously known IMBH candidates.

Regarding the low $[\text{O III}]/\text{H}\beta$ composites, the majority of such objects in the Reines et al. study mingle with H II galaxies in the $[\text{S II}]/\text{H}\alpha$ and (when detected) $[\text{O I}]/\text{H}\alpha$ diagrams. Although arguments have been made that this circumstance might arise from a mixture of star formation and AGN activity (e.g., Kewley et al. 2006), the fact that non-AGN processes can also lead to enhancements of low-ionization forbidden lines implies that the $[\text{N II}]/\text{H}\alpha$ ratio alone is not sufficient to confirm the presence of a massive black hole in these galaxies. Many of them — at least those within our redshift range that we have examined closely — have low emission-line luminosities that could be powered by stellar processes (e.g., photoionization by evolved stars; see Binette et al. 1994).

We also have excluded ambiguous objects that, when all available spectral evidence is considered, are more likely to be star-forming galaxies than AGNs. Objects in this category often have very weak low-ionization forbidden lines, but their high $[\text{O III}]/\text{H}\beta$ ratios place them close to (or just over) the maximal starburst lines on diagnostic diagrams. In some cases, the ratios may be consistent with those of low-metallicity AGNs. But in our sample, all such objects clearly have stellar continua in both the optical, where O and B stars dominate, and the far UV, where, based on their low starburst-like He II $\lambda 4686$ fluxes, a very steep continuum slope of $\alpha_{\text{UV}} = 4\text{--}5$ is indicated. As the helium abundance has only a weak dependence on metallicity (Groves et al. 2006), we expect that the He II/ $\text{H}\beta$ ratios of true low-metallicity AGNs should exceed those of starbursts. A few objects with these spectral characteristics are tentatively identified as pure AGNs in the Reines et al. (2013) sample (e.g., J0823+0313 and J0840+4707).

The other class of star-forming galaxies that we have excluded are those with starburst-like narrow-line flux ratios and broad $\text{H}\alpha$ emission. In principle, some of these could be extreme composite objects where the broad Balmer lines are the only AGN features not masked by the starburst. However, this is by no means the only possible interpretation, as some nearby extragalactic H II regions are known to display broad $\text{H}\alpha$ emission. One example is NGC 5471, which is located ~ 25 kpc from the center of M 101 and is not suspected of harboring an IMBH. Nevertheless, the luminosity and velocity width of the $\text{H}\alpha$ line in this object ($L_{\text{H}\alpha} = 2 \times 10^{38}$ ergs s^{-1} and $\text{FWHM}(\text{H}\alpha) = 1500$ km s^{-1} ; Isotov et al. 2007) imply a virial black-hole mass (via Xiao et al. 2011) of $\log(M_{\text{BH}}/M_{\odot}) = 5.1$, which would represent 10–50% of the mass of the entire stellar cluster in NGC 5471 (García-Benito et al. 2011). Along similar lines, some of the star-forming galaxies with broad $\text{H}\alpha$ emission in the Reines et al. (2013) sample (e.g., objects B, D, and H in their Tables 3 and 6) have estimated black-hole masses that are $\sim 1\%$ of the total stellar mass of the host galaxy — potentially very important in terms of galaxy/black hole co-evolution, or an indication that the broad $\text{H}\alpha$ emission is unrelated to the presence of a black hole. In the absence of other AGN indicators, vigorous star formation seems to offer the more straightforward explanation for such objects.

5.5. Notes on Individual Objects

J0948+0958: This galaxy has two superposed foreground stars and it lies $\sim 1'$ from a very bright star. We also noticed that the model magnitudes are significantly brighter (~ 0.4 mag in g) than the Petrosian magnitudes. We thus performed our own aperture photometry of the galaxy in the SDSS images with the *phot* task in IRAF, using a local background (measured at the same radius from the bright star as the galaxy) and removing the contribution of the foreground stars. We obtained magnitudes in g , r , and i that are within a few hundredths of a magnitude of the model magnitudes for the galaxy, so we have adopted the latter for our calculations.

J0949+3213: This object, also known as NGC 3011 and (more noteworthy) Mrk 409, is included in the Markarian survey of ultraviolet-excess galaxies. Interestingly, it has been classified repeatedly as a starburst galaxy in the literature (e.g., Balzano 1983; Salzer et al. 1995). Indeed, the object has a prominent blue star-forming ring located just outside the nucleus (Gil de Paz et al. 2003; see our Fig. 4). However, the SDSS spectrum leaves no question about the nature of the nuclear activity of this galaxy. In addition to narrow emission-line flux ratios that place it well within the Seyfert regions on the diagnostic diagrams in Figure 5 (particularly on the [O I]/H α plot), the object has strong He II $\lambda 4686$ emission.

J1109+6123: As mentioned above, this is the one galaxy that is common to our sample and that of Barth et al. (2008). Note that because our methods for estimating distances, stellar masses, and emission-line luminosities are not identical, the parameters listed in Tables 1 and 2 differ somewhat with those published by Barth et al. Our value of M_\star agrees closely with the revised stellar mass computed by Thornton et al. (2009).

J1207+4307: Also known as NGC 4117, this object was identified early on as a Seyfert galaxy (Huchra et al. 1982) despite having a rather low (compared to classical Seyferts) [N II]/H α ratio. In our sample, it has the weakest detected He II emission, but its [O I] strength (relative to H α) is second only to that of NGC 4395. In fact, on the [O I]/H α plot in Figure 5, NGC 4117 falls on the boundary between Seyferts and LINERs proposed by Kewley et al. (2006). It is, however, a bright X-ray source with an absorption column density ($N_{\text{H}} = 4 \times 10^{23} \text{ cm}^{-2}$; Cardamone et al. 2007) similar to that commonly observed in the X-ray spectra of luminous type 2 Seyfert nuclei. Thus, there is no question that this object is powered by black-hole accretion.

J1225+0519: This galaxy formally falls within the coordinate boundaries and velocity range often used to define membership in the Virgo cluster (Mould et al. 2000). Hence, it is also known as VCC 764. However, if the galaxy were in the cluster and at a distance of ~ 14 Mpc, it would have by far the faintest absolute magnitude and lowest stellar mass of any object our AGN sample. Given that the SDSS redshift is close to the upper limit assumed for Virgo membership, we considered the possibility that the galaxy is instead behind Virgo and computed its infall-corrected distance accordingly. This distance, 33.4 Mpc, implies a nuclear luminosity and host-galaxy properties that are much more in line with the rest of our sample, so we have adopted it here.

J1225+3332: This galaxy (NGC 4395), being the nearest and (in an angular sense) most extended object in our sample, requires special consideration in terms of its distance, photometry, and spectral analysis. We adopt the Cepheid distance of 4.3 Mpc for this galaxy (Thim et al. 2004), which is far more accurate than its redshift-based distance. Also, because the object is both extended and knotty, all Petrosian and model magnitudes listed in the DR7 and DR8 are much too faint. We have instead used the B and V magnitudes from the RC3 (de Vaucouleurs et al. 1991) and 2MASS K magnitude (Jarrett et al. 2003) to estimate its host-galaxy properties. We calculated the galaxy’s stellar mass using the BVK magnitudes and the appropriate coefficients from Bell et al. (2003). The absolute g -band magnitude listed in Table 1 was computed from these data using the transformations of R. Lupton (2005).⁶ The same transformations imply a $g - r$ color of 0.249, which we used to determine the location of this object in Figure 8.

Also, because the galaxy is so nearby and has a faint central surface brightness, the SDSS spectrum appears to contain light only from the nucleus. It is the only object in our sample for which a pure power law was used to model the continuum.

J1351+4012: As discussed above, this object is a good candidate for a Seyfert/starburst composite galaxy based on its emission-line flux ratios. Similar to J0949+3213, it is a UV-excess Markarian galaxy (Mrk 462) with a compact, blue central region that suggests active star formation. However, as noted in § 5.1, other spectral evidence points strongly to the presence of an accreting black hole. Its only published spectral classification is that of “emission spectrum galaxy” (Petrosian et al. 2007).

J1448+1227: This galaxy, also known as NGC 5762, has been studied because of its 21 cm neutral hydrogen emission (Lewis et al. 1985; Rosenberg et al. 2000) and active star-formation (e.g., Kewley et al. 2002; note its blue, H II region-studded disk in Fig. 4). Interestingly, little attention has been given to its nuclear properties. The continuum in the SDSS spectrum is dominated by light from an older stellar population, and the emission-line flux ratios are clearly those of a type 2 Seyfert.

J1605+0850: Although the DR7 Petrosian and model magnitudes for this galaxy are similar, the radius of the region used for the aperture photometry is much smaller than its total optical extent ($\sim 4''$ vs. $\sim 12''$), meaning all of the DR7 magnitudes are too faint. As with J0948+0958, this galaxy lies within $1'$ of a bright foreground star, which may have affected the sky subtraction. Regardless, the problem seems to have been corrected in the DR8 — our manually measured magnitudes (following the method described above for J0948+0958) agree well with the DR8 Petrosian magnitudes, so we have adopted the latter for our analysis.

⁶See <http://www.sdss.org/dr7/algorithms/sdssUBVRITransform.html>

6. Summary and Conclusions

Nearby dwarf galaxies with intermediate-mass black holes afford a glimpse into the earlier stages of black hole/galaxy co-evolution. Owing to the fact that both components have undergone relatively little growth over cosmic time, dwarf galaxy AGNs also provide an opportunity to discriminate between models for the formation of massive black-hole seeds — a population which, at present, does not lend itself to direct observational study. Using a distance-limited portion of the SDSS DR7, we have assembled a sample of 28 AGNs within ~ 80 Mpc that reside in galaxies with stellar masses less than $10^{10} M_{\odot}$ (calculated via the Bell et al. 2003 method). As we have excluded emission-line galaxies that could be powered by stellar processes, these objects are the least massive galaxies in the very local universe certain to contain central black holes. We estimate that ~ 75 – 80% of all nearby galaxies with similar absolute magnitudes ($M_g \approx -17$ to -18) have SDSS spectra (E. Moran et al. 2015, in preparation), implying that the completeness of our optically selected sample is high.

We began the process of constructing this sample by treating every galaxy with a nuclear SDSS spectrum that falls within our adopted distance limit as a potential AGN host. We then carefully modeled the stellar continua of the objects, combining automatic emission-line measurements with visual assessments of the continuum-subtracted spectra, to classify the type of activity present. By focusing on the nearest galaxies and not imposing explicit S/N ratio or equivalent width limits on the diagnostic emission lines, this approach has yielded a sample of AGNs with very low luminosities and host-galaxy masses. As a result, our survey is less affected by luminosity bias than previous SDSS searches for IMBH candidates. The low fraction of objects with previous X-ray or radio detections suggests that optical spectroscopy is the most economical way to identify low-luminosity active nuclei in dwarf galaxies.

Based on the SDSS spectra, the vast majority of AGNs in our sample appear to be narrow-line (type 2) objects. Although the non-uniform quality of the data prevents us from drawing firm conclusions about the true ratio of narrow- and broad-line AGNs at low luminosities, there is nothing about our selection methods that would have caused us to miss obvious type 1 objects. We are currently obtaining high S/N ratio follow-up spectra, in part so that we may place tighter constraints on the broad-line AGN fraction for this sample. In addition, we have obtained X-ray data for a subset of the objects to search for evidence of heavy absorption in the type 2 objects similar to that observed in classical Seyfert 2 nuclei. Obscured or not, the low nuclear luminosities displayed by our sample imply low minimum black hole masses in the $\sim 10^3 - 10^4 M_{\odot}$ range, which is approximately where the initial mass functions predicted for different black-hole seed formation scenarios overlap the most (e.g., Volonteri 2010).

Although many of the host galaxies of the AGNs we have found appear to be disk-dominated systems, most of them are not blue, dwarf spirals similar to the original IMBH host, NGC 4395. One possibility is that, at the lower nuclear luminosities exhibited in our sample, we include more typical members of the IMBH population, which in turn are found in the more typical host galaxies

of such objects. Alternatively, the low incidence of vigorous star formation amongst the AGN hosts might be a reflection of the fact that, at low luminosity, the emission-line signatures of black-hole accretion are more easily masked by emission from circumnuclear star-forming regions. If so, high spatial resolution spectroscopy of blue, low-mass galaxies (especially those that display ambiguous features in their SDSS spectra) and searches for non-optical AGN emission in these objects could provide a more complete census of IMBHs and their host galaxies.

There is a general impression that AGNs in low-mass galaxies are rare (e.g., see Kauffmann et al. 2003). If this is the case, then new, nearby examples such as those presented here will be valuable additions for investigations into the relationship between black holes and galaxies. However, we note that an appearance of rareness is likely to occur in AGN samples that are biased in favor of high-luminosity objects; AGN fractions derived from surveys that emphasize low-luminosity objects should be more accurate. In this study, if we examine just the $M_{\star} = (4 - 10) \times 10^9 M_{\odot}$ range — which is free of significant incompleteness (Fig. 1b) and includes 75% of the AGN host galaxies in our survey (Fig. 8) — we obtain an AGN fraction of 2.7%. This fraction increases to 5.0% if we only consider objects in the color range exhibited by the AGNs (i.e., $g - r = 0.5 - 0.8$). The latter figure is probably optimistic, but not entirely so if circumnuclear star formation has affected our ability to detect AGNs in bluer galaxies. Although much more work lies ahead — developing truly complete samples and a gaining a better handle on the limitations of optical spectroscopy — AGN fractions in this range are becoming relevant in terms of the predicted black-hole occupation fractions expected for galaxies of this mass.

Generous support for this work was provided by the National Science Foundation through grant AST-0909063. We are very grateful to the referee, Jenny Greene, for her thorough and insightful review of this article, which helped us to make a number of valuable improvements. We would also like to thank Michele Cappellari for providing access to the pPXF code, and Marc Sarzi for sharing the GANDALF software and for his time during numerous conversations regarding its inner workings. This research has made use of a number of other publicly available resources, for which we are grateful: synthetic stellar population models from the MILES team; the NASA/IPAC Extragalactic Database (NED), which is operated by the Jet Propulsion Laboratory, California Institute of Technology; the K -correction calculator of I. Chilingarian and colleagues; and of course, the photometric and spectroscopic databases from the SDSS collaboration. E.C.M. would like to express special thanks to Meg Urry and the staff of the Yale Center for Astronomy and Astrophysics for their hospitality during a sabbatical visit, when much of the work presented here was completed. M.E. would like to thank the Center for Relativistic Astrophysics at Georgia Tech and the Department of Astronomy at the University of Washington for their warm hospitality during the last stages of his work on this paper.

REFERENCES

- Abazajian, K. N., Adelman-McCarthy, J. K., Agüeros, M. A., et al. 2009, *ApJS*, 182, 543
- Aihara, H., Allende Prieto, C., An, D., et al. 2011, *ApJS*, 193, 29
- Antonucci, R. 1993, *ARA&A*, 31, 473
- Araya Salvo, C., Mathur, S., Ghosh, H., Fiore, F., & Ferrarese, L. 2012, *ApJ*, 757, 179
- Balzano, V. A. 1983, *ApJ*, 268, 602
- Barth, A. J., Greene, J. E., & Ho, L. C. 2005, *ApJ*, 619, L151
- Barth, A. J., Greene, J. E., & Ho, L. C. 2008, *AJ*, 136, 1179
- Barth, A. J., Ho, L. C., Rutledge, R. E., & Sargent, W. L. W. 2004, *ApJ*, 607, 90
- Becker, R. H., White, R. L., & Helfand, D. J. 1995, *ApJ*, 450, 559
- Bell, E. F., McIntosh, D. H., Katz, N., & Weinberg, M. D. 2003, *ApJS*, 149, 289
- Bentz, M. C., Peterson, B. M., Pogge, R. W., & Vestergaard, M. 2009, *ApJ*, 694, L166
- Binette, L., Magris, C. G., Stasińska, G., & Bruzual, A. G. 1994, *A&A*, 292, 13
- Bromm, V., Coppi, P. S., & Larson, R. B. 1999, *ApJ*, 527, L5
- Cappellari, M., & Emsellem, E. 2004, *PASP*, 116, 138
- Cardamone, C. N., Moran, E. C., & Kay, L. E. 2007, *AJ*, 134, 1263
- Chilingarian, I. V., Melchior, A.-L., & Zolotukhin, I. Y. 2010, *MNRAS*, 405, 1409
- de Vaucouleurs, G., de Vaucouleurs, A., Corwin, H. G., Jr., Buta, R. J., Paturel, G., & Fouqué, P. 1991, *Third Reference Catalog of Bright Galaxies*, (New York: Springer-Verlag)
- Desroches, L.-B., & Ho, L. C. 2009, *ApJ*, 690, 267
- Di Matteo, T., Springel, V., & Hernquist, L. 2005, *Nature*, 433, 604
- Dong, X.-B., Ho, L. C., Yuan, W., et al. 2012, *ApJ*, 755, 167
- Dong, X., Wang, T., Yuan, W., et al. 2007, *ApJ*, 657, 700
- Dopita, M. A., & Sutherland, R. S. 1995, *ApJ*, 455, 468
- Eracleous, M., & Halpern, J. P. 2001, *ApJ*, 554, 240
- Eracleous, M., Hwang, J. A., & Flohic, H. M. L. G. 2010, *ApJ*, 711, 796
- Ferrarese, L. 2004, in *Supermassive Black Holes in the Distant Universe*, ed. A. J. Barger, (Dordrecht: Kluwer), 1
- Ferland, G. J., & Netzer, H. 1983, *ApJ*, 264, 105
- Ferrarese, L., & Merritt, D. 2000, *ApJ*, 539, L9
- Filippenko, A. V., & Halpern, J. P. 1984, *ApJ*, 285, 458
- Filippenko, A. V., & Ho, L. C. 2003, *ApJ*, 588, L13

- Filippenko, A. V., & Sargent, W. L. W. 1989, *ApJ*, 342, L11
- Filippenko, A. V., & Terlevich, R. 1992, *ApJ*, 397, L79
- Gallo, E., Treu, T., Jacob, J., et al. 2008, *ApJ*, 680, 154
- García-Benito, R., Pérez, E., Díaz, Á. I., Maíz Apellániz, J., & Cerviño, M. 2011, *AJ*, 141, 126
- Gebhardt, K., Bender, R., Bower, G., et al. 2000, *ApJ*, 539, L13
- Gebhardt, K., Lauer, T. R., Kormendy, J., et al. 2001, *AJ*, 122, 2469
- Gil de Paz, A., Madore, B. F., Noeske, K., et al. 2003, *ApJ*, 596, L179
- Greene, J. E., & Ho, L. C. 2004, *ApJ*, 610, 722
- Greene, J. E., & Ho, L. C. 2007a, *ApJ*, 667, 131
- Greene, J. E., & Ho, L. C. 2007b, *ApJ*, 670, 92
- Greene, J. E., Ho, L. C., & Barth, A. J. 2008, *ApJ*, 688, 159
- Groves, B. A., Dopita, M. A., & Sutherland, R. S. 2004, *ApJS*, 153, 9
- Groves, B. A., Heckman, T. M., & Kauffmann, G. 2006, *MNRAS*, 371, 1559
- Gültekin, K., Richstone, D. O., Gebhardt, K., et al. 2009, *ApJ*, 698, 198
- Halpern, J. P., & Steiner, J. E. 1983, *ApJ*, 269, L37
- Heckman, T. M., Kauffmann, G., Brinchmann, J., et al. 2004, *ApJ*, 613, 109
- Ho, L. C. 2008, *ARA&A*, 46, 475
- Ho, L. C., Filippenko, A. V., & Sargent, W. L. W. 2003, *ApJ*, 583, 159
- Hopkins, P. F., Hernquist, L., Cox, T. J., et al. 2005, *ApJ*, 630, 705
- Huchra, J. P., Wyatt, W. F., & Davis, M. 1982, *AJ*, 87, 1628
- Izotov, Y. I., Thuan, T. X., & Guseva, N. G. 2007, *ApJ*, 671, 1297
- Jardel, J. R., & Gebhardt, K. 2012, *ApJ*, 746, 89
- Jarrett, T. H., Chester, T., Cutri, R., Schneider, S. E., & Huchra, J. P. 2003, *AJ*, 125, 525
- Jiang, Y.-F., Greene, J. E., Ho, L. C., Xiao, T., & Barth, A. J. 2011, *ApJ*, 742, 68
- Karachentsev, I. D., & Makarov, D. A. 1996, *AJ*, 111, 794
- Kauffmann, G., Heckman, T. M., Tremonti, C., et al. 2003, *MNRAS*, 346, 1055
- Kormendy, J., & Richstone, D. 1995, *ARA&A*, 33, 581
- Kewley, L. J., Dopita, M. A., Sutherland, R. S., Heisler, C. A., & Trevena, J. 2001, *ApJ*, 556, 121
- Kewley, L. J., Geller, M. J., Jansen, R. A., & Dopita, M. A. 2002, *AJ*, 124, 3135
- Kewley, L. J., Groves, B., Kauffmann, G., & Heckman, T. 2006, *MNRAS*, 372, 961
- Kroupa, P. 2001, *MNRAS*, 322, 231
- Lewis, B. M., Helou, G., & Salpeter, E. E. 1985, *ApJS*, 59, 161

- Lodato, G., & Natarajan, P. 2006, MNRAS, 371, 1813
- Lora, V., Sánchez-Salcedo, F. J., Raga, A. C., & Esquivel, A. 2009, ApJ, 699, L113
- Ludwig, R. R., Greene, J. E., Barth, A. J., & Ho, L. C. 2012, ApJ, 756, 51
- Maiolino, R., & Rieke, G. H. 1995, ApJ, 454, 95
- Marconi, A., & Hunt, L. K. 2003, ApJ, 589, L21
- McAlpine, W., Satyapal, S., Gliozzi, M., et al. 2011, ApJ, 728, 25
- Mickaelian, A. M., Hovhannisyan, L. R., Engels, D., Hagen, H.-J., & Voges, W. 2006, A&A, 449, 425
- Moran, E. C. 2010, BAAS, 42, 597
- Moran, E. C., Filippenko, A. V., Ho, L. C., et al. 1999, PASP, 111, 801
- Mould, J. R., Huchra, J. P., Freedman, W. L., et al. 2000, ApJ, 529, 786
- Nardini, E., & Risaliti, G. 2011, MNRAS, 417, 2571
- Neumayer, N., & Walcher, C. J. 2012, Adv. Astron., 2012:709038
- Oh, K., Sarzi, M., Schawinski, K., & Yi, S. K. 2011, ApJS, 195, 13
- Osterbrock, D. E. 1989, *Astrophysics of Gaseous Nebulae and Active Galactic Nuclei* (Mill Valley, CA: Univ. Science Books)
- Osterbrock, D. E., & Shaw, R. A. 1988, ApJ, 327, 89
- Penston, M. V., & Fosbury, R. A. E. 1978, MNRAS, 183, 479
- Peterson, B. M., Bentz, M. C., Desroches, L.-B., et al. 2005, ApJ, 632, 799
- Petrosian, A., McLean, B., Allen, R. J., & MacKenty, J. W. 2007, ApJS, 170, 33
- Reines, A. E., Greene, J. E., & Geha, M. 2013, ApJ, 775, 116
- Reines, A. E., Sivakoff, G. R., Johnson, K. E., & Brogan, C. L. 2011, Nature, 470, 66
- Rosenberg, J. L., & Schneider, S. E. 2000, ApJS, 130, 177
- Salzer, J. J., Moody, J. W., Rosenberg, J. L., Gregory, S. A., & Newberry, M. V. 1995, AJ, 109, 2376
- Sarzi, M., Falcón-Barroso, J., Davies, R. L., et al. 2006, MNRAS, 366, 1151
- Sarzi, M., Shields, J. C., Pogge, R. W., & Martini, P. 2007, in *The Central Engine of Active Galactic Nuclei*, eds. L. C. Ho & J.-M. Wang, (San Francisco: ASP), 643
- Schlafly, E. F., & Finkbeiner, D. P. 2011, ApJ, 737, 103
- Schramm, M., Silverman, J. D., Greene, J. E., et al. 2013, ApJ, 773, 150
- Secrest, N. J., Satyapal, S., Gliozzi, M., et al. 2012, ApJ, 753, 38
- Seth, A. C., Cappellari, M., Neumayer, N., et al. 2010, ApJ, 714, 713

- Shields, J. C. 1992, *ApJ*, 399, L27
- Skrutskie, M. F., Cutri, R. M., Stiening, R., et al. 2006, *AJ*, 131, 1163
- Thim, F., Hoessel, J. G., Saha, A., et al. 2004, *AJ*, 127, 2322
- Thornton, C. E., Barth, A. J., Ho, L. C., & Greene, J. E. 2009, *ApJ*, 705, 1196
- Thornton, C. E., Barth, A. J., Ho, L. C., Rutledge, R. E., & Greene, J. E. 2008, *ApJ*, 686, 892
- Tremaine, S., Gebhardt, K., Bender, R., et al. 2002, *ApJ*, 574, 740
- Tremonti, C. A., Heckman, T. M., Kauffmann, G., et al. 2004, *ApJ*, 613, 898
- Ulvestad, J. S., & Wilson, A. S. 1989, *ApJ*, 343, 659
- Valluri, M., Ferrarese, L., Merritt, D., & Joseph, C. L. 2005, *ApJ*, 628, 137
- Vazdekis, A., Sánchez-Blázquez, P., Falcón-Barroso, J., et al. 2010, *MNRAS*, 404, 1639
- Veilleux, S. 1991, *ApJ*, 369, 331
- Veilleux, S., & Osterbrock, D. E. 1987, *ApJS*, 63, 295
- Volonteri, M. 2010, *A&A Rev.*, 18, 279
- Volonteri, M., Haardt, F., & Madau, P. 2003, *ApJ*, 582, 559
- Volonteri, M., Lodato, G., & Natarajan, P. 2008, *MNRAS*, 383, 1079
- Xiao, T., Barth, A. J., Greene, J. E., et al. 2011, *ApJ*, 739, 28
- Yan, R., & Blanton, M. R. 2012, *ApJ*, 747, 61